



HAL
open science

The hydrothermal alkaline alteration of potassium feldspar: A nanometer-scale investigation of the orthoclase interface

Roland Hellmann, Yuanyuan Zhai, Eric Robin, Nathaniel Findling, Sathish Mayanna, Richard Wirth, Anja Schreiber, Martiane Cabié, Qingdong Zeng, Shanke Liu, et al.

► To cite this version:

Roland Hellmann, Yuanyuan Zhai, Eric Robin, Nathaniel Findling, Sathish Mayanna, et al.. The hydrothermal alkaline alteration of potassium feldspar: A nanometer-scale investigation of the orthoclase interface. *Chemical Geology*, 2021, 569, pp.120133. 10.1016/j.chemgeo.2021.120133 . hal-03389010

HAL Id: hal-03389010

<https://hal.science/hal-03389010v1>

Submitted on 22 Oct 2021

HAL is a multi-disciplinary open access archive for the deposit and dissemination of scientific research documents, whether they are published or not. The documents may come from teaching and research institutions in France or abroad, or from public or private research centers.

L'archive ouverte pluridisciplinaire **HAL**, est destinée au dépôt et à la diffusion de documents scientifiques de niveau recherche, publiés ou non, émanant des établissements d'enseignement et de recherche français ou étrangers, des laboratoires publics ou privés.

The hydrothermal alkaline alteration of potassium feldspar: a nanometer-scale investigation of the orthoclase interface

Roland Hellmann^{*a}, Yuanyuan Zhai^{b,c,d,1}, Eric Robin^e, Nathaniel Findling^a, Sathish Mayanna^{f,2}, Richard Wirth^f, Anja Schreiber^f, Martiane Cabié^g, Qingdong Zeng^{b,c,d}, Shanke Liu^{b,c}, Jianming Liu^{b,c,d,3}.

^aUniversité Grenoble Alpes and CNRS, ISTERre, F-38058 Grenoble Cedex 9, France

^bKey Laboratory of Mineral Resources, Institute of Geology and Geophysics, Chinese Academy of Sciences, Beijing 100029, China

^cInnovation Academy for Earth Science, Chinese Academy of Sciences, Beijing 100029, China

^dCollege of Earth Sciences, University of Chinese Academy of Sciences, Beijing 100049, China

^eUniversité Grenoble Alpes, IRIG, MEM, CEA, Grenoble, France

^fHelmholtz Centre Potsdam, GFZ Deutsches GeoForschungsZentrum, Interface Geochemistry Sektion 3.5, Telegrafenberg, D-14473 Potsdam, Germany

^gAix Marseille Université, CNRS, Centrale Marseille, FSCM (FR1739), CP2M, F-13397 Marseille, France

¹ current address: Shenzhen Xinhua Middle School, Shenzhen 518109, China

² current address: Carl Zeiss Microscopy GmbH, D-73447 Oberkochen, Germany

³ retired

Key words: orthoclase feldspar alkaline hydrothermal alteration, coupled interfacial dissolution-precipitation (CIDR), analytical transmission electron microscopy (TEM), energy filtered TEM (EFTEM), TEM-EDXS, electron energy loss spectroscopy (EELS), orthoclase-fluid interface, secondary cement phases, CASH and CSH, K fertilizer

*to whom correspondence may be addressed.

Email: roland.hellmann@univ-grenoble-alpes.fr

ABSTRACT

Potassium feldspars (KAlSi_3O_8) are ubiquitous minerals in the Earth's upper crust. This family of minerals has been the subject of numerous experimental and theoretical investigations concerning their dissolution kinetics and the mechanisms controlling chemical alteration at acid and neutral pH, and at temperatures ranging from ambient to hydrothermal conditions. On the other hand, considerably less research on the dissolution behavior of K-feldspars has been carried out at alkaline conditions, in particular at $\text{pH} > 9$ and elevated temperatures. Filling in this gap in knowledge is the major motivation for this study. More specifically, we wanted to document and understand how the K-feldspar interface structurally and chemically evolves during alteration in order to determine the mechanism of dissolution. In this study we examined interfaces of orthoclase samples that were altered in separate experiments in a $\text{Ca}(\text{OH})_2\text{-H}_2\text{O}$ solution ($\text{pH}_{25^\circ\text{C}} 12.4$) at 190°C for 24 hours. We used a combination of focused ion beam (FIB) milling and advanced analytical transmission electron microscopy (TEM) techniques to investigate the structure and chemistry of the near surface region of post-reaction grains, with particular attention being given to the fluid-solid interface. Even though each grain diminishes in volume due to dissolution, high-resolution TEM imaging indicates that the feldspar structure itself remains completely intact and crystalline, as evidenced by lattice fringes that abruptly terminate at the grain edge. Nanometer-scale chemical composition measurements and mapping by TEM-EDXS (energy dispersive X-ray spectroscopy) and EFTEM (energy filtered TEM) show that the chemistry of the parent feldspar also remains unchanged at the interface. In particular, there is no evidence for the incursion of Ca from the fluid solvent into the structure, either by interdiffusion or by a replacement process. Taken together, the TEM observations point to a sharp chemical reaction front characterized by the congruent (i.e. stoichiometric) release of all elements from the feldspar structure.

Nanometer-scale measurements by high resolution analytical TEM also reveal that a surface alteration layer (SAL) of amorphous material forms in situ at the expense of the feldspar structure. The interface demarcates a spatially coincident and nm-sharp chemical and structural discontinuity between the parent feldspar and the amorphous phase. The amorphous SAL has a variable thickness, from under 10 nm up to ~ 200 nm. This is likely one of the first observed occurrences of a significant surface amorphous layer on feldspar due to alteration in an alkaline solvent. The lack of a gap between the two phases points to an interfacial dissolution-precipitation process that continuously operates during hydrothermal alteration, and mostly likely right from the onset of contact with the fluid. After the initial formation of the amorphous layer, a 1-2 μm -thick porous amalgam of secondary crystalline phases comprised of calcite, tobermorite, and hydrogrossular, as well as other minor phases, precipitated over

65 the SAL. These authigenic crystalline minerals formed during the experiment (hydrothermal alteration,
66 followed by fluid loss due to evaporation) by a classical thermodynamically-controlled precipitation
67 process as the reactor bulk fluid became increasingly concentrated.

68 We propose that a coupled interfacial dissolution-reprecipitation (CIDR) mechanism best
69 explains the chemical and structural properties of the interface and the formation of an amorphous
70 surface layer. In fact, many recent studies postulate that a CIDR process controls feldspar dissolution
71 and the formation of SALs at acid and circumneutral pH over a wide range of temperatures. Combining
72 these previous results with our new observations supports the idea that a unique and unifying mechanism
73 likely controls chemical alteration of feldspars in all aqueous fluids.

74

75

76 **1 INTRODUCTION**

77 **1.1. Research goals**

78

79 The feldspar-water system is arguably one of the most important in the earth sciences, in
80 particular with respect to chemical weathering associated with water-rock interactions. This is primarily
81 due to the preponderance of feldspar minerals in the upper continental crust and at earth's surface (Klein
82 and Philpotts, 2017). Feldspars are chemically robust framework silicates and thus dissolve very slowly,
83 with the kinetics of dissolution depending strongly on pH and temperature. While the aqueous alteration
84 of feldspars has been extensively investigated experimentally and theoretically, the overwhelming
85 majority of studies have focused on alteration at conditions encompassing acid, circumneutral, and weak
86 alkaline pH conditions (i.e., pH 1-9), and at temperatures less than 100 °C. There are several reviews of
87 feldspar dissolution rates as a function of pH at ambient conditions, e.g., Blum and Stillings, 1995;
88 Bandstra et al., 2008; at elevated temperatures up to hydrothermal conditions, see, e.g., Hellmann, 1994;
89 Yuan et al., 2019; and references therein. The review of feldspar alteration by Yuan et al. (2019) is a
90 good starting point for a synopsis of both new and not-so-recent work concerning both dissolution rates
91 and mechanisms of feldspar alteration reactions in aqueous fluids.

92 In this study we examine post-reaction solid-fluid interfaces of alkali feldspars in order to
93 elucidate the mechanism of chemical alteration in alkaline aqueous fluids with a very high pH. As
94 discussed in more detail in section 1.3, it is at these conditions where there is a real need for more
95 experimental data, which in turn explains one of the motivations for our research. Moreover, we wanted
96 to document and understand how the crystal structure evolves both structurally and chemically when in
97 contact with a very basic pH solution at elevated temperature. Many studies have reported the formation

98 of surface altered layers (SALs) on feldspars undergoing chemical alteration at acid, circumneutral, and
99 mild alkaline conditions (e.g., Hellmann et al. 2003, 2012; and references therein), We note, however,
100 that literature data on feldspar hydrolysis at basic pH conditions ($> \text{pH } 9$) are not numerous, this in
101 particular being true for temperatures above $100\text{ }^{\circ}\text{C}$. For this reason we posed the question whether this
102 interfacial process, in other words SAL formation, also operates when an alkali feldspar is exposed to an
103 aggressive basic pH solution at elevated temperature. In response to this question, the present research is
104 among the first that has focused on a detailed structural and chemical examination of feldspar interfaces
105 after basic pH alteration using high-resolution analytical TEM techniques.

106 The overarching goal of our study was to focus on nanometer-scale TEM measurements to
107 characterize structural and chemical changes to the interfacial region that encompasses the near surface
108 of the primary feldspar and abutting authigenic secondary phases. We were in particular interested in
109 two elements, K and Ca. The behavior of K is fundamental, as it is a good tracer element for following
110 the overall hydrothermal alteration process, starting with its release during dissolution of the parent
111 feldspar, and then understanding its distribution with respect to the precipitation of secondary authigenic
112 phases (see e.g., Zhai et al., 2021). On the other hand, determining the mobility and distribution of Ca is
113 primordial since $\text{Ca}(\text{OH})_2$ makes up the solvent, and thus it is important to measure its distribution at
114 high spatial resolution in order to determine whether or not it penetrates into the orthoclase structure. In
115 addition, important framework elements, such as Si, Al, and O, were also measured by TEM. Taken
116 together, our TEM data provided us with the means to propose an operative mechanism at the
117 nanometer-scale for K-feldspar alteration at basic pH.

118 Even though the present research is uniquely devoted to orthoclase feldspar, it is worth
119 reiterating that there are 3 common alkali feldspar polymorphs that share the same nominal formula,
120 KAlSi_3O_8 . However, their atomic structures are not identical. Sanidine is the polymorph that forms at
121 the highest temperature and fastest cooling rates, whereas orthoclase and microcline crystallize at lower
122 temperatures and are characterized by much slower cooling rates. The temperature and rate of
123 crystallization affects the degree of Al/Si ordering on the tetrahedral sites, with sanidine displaying the
124 highest disorder, and microcline the lowest. Both sanidine and orthoclase crystallize in the monoclinic
125 system (H-M, class $2/m$), while microcline crystallizes in the triclinic system (class $\bar{1}$). Classical studies,
126 such as by Brown and Parsons, 1989, have addressed important processes that include ordering rates and
127 phase transformations of the various K-feldspar polymorphs. These phenomena are intimately related to
128 the creation of internal microstructures, which in turn can affect global dissolution behavior. While
129 important for controlling the overall kinetics of K-feldspar dissolution, quantifying the effects of
130 crystallographic structures at the micrometer to sub-micrometer-scale, as well as the degree of Al/Si

131 ordering, was not an objective of this study (for the effects of ordering on dissolution, see, e.g., Yang et
132 al., 2013, 2014a,b). In addition, a detailed mineralogical-crystallographic characterization of the
133 hydrothermal secondary products was also not carried out here. Nonetheless, another study on
134 hydrothermally altered microcline and sanidine focuses on the distribution and concentrations of
135 released K in secondary authigenic phases (Zhai et al., 2021).

136

137 **1.2. Brief review of surface alteration processes**

138 One of the key aspects for elucidating the mechanism of dissolution of any primary crystalline or
139 glassy phase is a detailed understanding of surface altered layers that typically form in situ on a
140 retreating (dissolving) surface. This involves using high-resolution analytical techniques in order to
141 measure their chemistry and structure, as well as the respective interfacial gradients with the parent
142 phase (e.g., see Hellmann et al., 2003, 2012, 2015). These layers are amorphous and generally have a
143 chemical composition distinct from the parent mineral (or glass). Many recent studies on feldspars
144 altered at acid to circumneutral pH conditions, in both the laboratory and in the field, have documented
145 their presence using TEM techniques (e.g., Hellmann et al., 2003, 2012; Lee et al., 2007, 2008;
146 references therein). In fact, nearly all polycationic silicate minerals have the potential to develop a SAL
147 when in contact with an aqueous fluid (Hellmann et al., 2012, Ruiz-Agudo et al., 2012). Related to SAL
148 formation is an equivalent process termed mineral-mineral replacement, but in this case a secondary
149 mineral replaces the primary mineral (see reviews in Putnis, 2009, 2014).

150 Traditional thinking regarding both SAL formation and mineral-mineral replacement posits that
151 they are controlled by an interdiffusion process between preferentially leached cations in the parent solid
152 and certain charge-compensating cations (including H_3O^+) in the bulk fluid (see reviews in Hellmann et
153 al., 2012; Yuan et al., 2019). However, based on the application of relatively new and advanced
154 analytical techniques to altered samples prepared in cross-section by ultramicrotomy (e.g., Thomassin et
155 al., 1995; Buck et al., 2000; Hellmann et al., 2003) and focused ion beam milling-FIB (e.g. Wirth, 2004;
156 Hellmann et al., 2012), the theory of preferential cation leaching controlled by interdiffusion has become
157 increasingly doubtful. In fact, research over the past two decades promotes an alternative theory that is
158 gaining widespread acceptance. It is based on a coupled interfacial process that links dissolution of the
159 parent mineral with the synchronous interfacial reprecipitation of a secondary phase, which can be either
160 amorphous (SAL) or crystalline. In the latter case, this is governed by a pseudomorphic replacement
161 process (Putnis, 2002, 2009, 2014; King et al., 2011). Some minerals, in particular feldspars, can
162 develop an amorphous SAL (Hellmann, et al., 2003, 2012), or alternatively, show replacement by a
163 feldspar of another composition (O'Neil and Taylor, 1967; Labotka et al., 2004; Hövelmann et al.,

164 2010). Both the nature of the primary mineral and the physicochemical conditions of the fluid determine
165 in large part which process occurs (see details in Hellmann et al., 2012- Fig. 4). It is important that SALs
166 and mineral-mineral replacement are not confused with the classical precipitation of secondary phases
167 onto a mineral surface from a chemically oversaturated bulk fluid. These points are discussed in more
168 detail further on.

169

170 **1.3 Previous Work**

171 It has commonly been assumed that feldspars, and silicate minerals in general, dissolve ‘more-or-
172 less’ congruently at ambient temperatures and at neutral to basic pH conditions, without the formation of
173 SALs. In regard to feldspars, this is based on aqueous chemistry measurements showing that non-
174 stoichiometric dissolution is most pronounced at acid pH conditions, and significantly less at
175 circumneutral and basic pH (Chou and Wollast, 1985; Holdren and Speyer, 1985; at elevated
176 temperatures, see e.g., Hellmann et al., 1989; Hellmann, 1999a,b). With the application of relatively new
177 solid-state analysis techniques in the geosciences, the formation of SALs on feldspars and other silicates
178 received much attention in the 1990’s and the decade thereafter. The pioneering studies by Petit and
179 Dran applied several types of surface sensitive multi-eV ion beam methods, such as resonant nuclear
180 reaction analysis (RNRA), to obtain H and cation depth profiles of chemically altered feldspars and
181 other silicate minerals and glasses (Petit et al., 1989, 1990a,b; Dran et al., 1988; Hellmann et al., 1997).
182 Casey and co-workers applied elastic recoil detection (ERD) and Rutherford backscattering
183 spectroscopy (RBS) to determine H and cation depth profiles on labradorite feldspar surfaces after
184 reaction at ambient or near-ambient temperatures over a wide range of solvent pH (Casey et al. 1988,
185 Casey et al., 1989a,b; Arnold et al., 2002).

186 Other surface-sensitive techniques, such as X-ray photoelectron spectroscopy (XPS) (Hellmann
187 et al., 1990; Chen et al., 2000) and secondary ion mass spectrometry (SIMS) (Schweda et al., 1997;
188 Nesbitt and Muir, 1988; Nugent et al., 1998) were also used to study cation depletion in reacted
189 feldspars as a function of pH and temperature. Other lesser known techniques, such as high-resolution
190 in-situ X-ray reflectivity (XR) and ex-situ X-ray reflection interface microscopy (XRIM), were used by
191 Fenter and colleagues to probe near-surface orthoclase chemistry after reaction at 25 and 50 °C in
192 solutions at acid, neutral, and very basic pH (Fenter et al., 2000, 2010; Teng et al., 2001).

193 When considered together, data from most of the above-cited studies indicate that changes in the
194 near surface of feldspars do occur during chemical alteration, both in terms of chemistry and the
195 formation of an amorphous SAL. With the exception of alteration at acid pH conditions, these SALS are
196 restricted to thicknesses of several molecular layers, which corresponds to the top most layers of the

197 former feldspar structure. Moreover, some of the above studies concluded that feldspars dissolve more
198 or less congruently at ≤ 50 °C at neutral to basic pH conditions, and that dissolution only proceeds at the
199 immediate surface, layer by layer. While SALs are undoubtedly thin at these pHs and low temperatures,
200 the top-down surface analytical techniques with large beam foot prints that were used in the 1990's and
201 early 2000's were also limited in sensitivity and/or spatial resolution. For this reason, the study of
202 reacted mineral interfaces prepared in cross section by ultramicrotomy (Thomassin et al., 1995;
203 Hellmann et al., 2003) or by FIB (e.g., Wirth, 2004) with Å-resolved TEM techniques has proven to be a
204 breakthrough and an enormous advantage for better characterizing altered surfaces and understanding
205 how they form, see e.g., Buck et al., 2000; Hellmann et al., 2003.

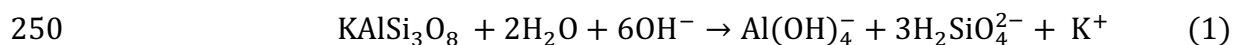
206 Up to the end of the 1990s only a handful of studies had been dedicated to alkaline hydrothermal
207 alteration of feldspars, in particular the detailed exploration of SALs and their mechanism of formation.
208 One pioneering study used XPS and angle-resolved XPS (ARXPS) to measure the near-surface
209 chemistry of albite ($\text{NaAlSi}_3\text{O}_8$) that had been subjected to hydrothermal alteration at 225 °C in a
210 $\text{pH}_{(25^\circ\text{C})}$ 10.1 solution (Hellmann et al., 1990). This study showed, via non-stoichiometric near-surface
211 Al/Si, Na/Si, and O/Si ratios, that SALs with thicknesses of many tens of nm form at these conditions.
212 The possibility of relatively thick SALs developing during alteration at basic pH and hydrothermal
213 conditions was further supported by results from an experimental study by Hellmann (1995), based on
214 alkaline dissolution of albite feldspars at $\text{pH}_{(25^\circ\text{C})}$ 10.0 and 12.0 at hydrothermal conditions (100, 200,
215 and 300 °C). Even though only aqueous solution compositions were measured, a generalized and
216 significant non-stoichiometry was reported. These results are tantalizing, in that they provide indirect
217 evidence for the formation of non-negligible SALs at elevated T and pH conditions. Even though these
218 experiments used pure albite feldspar ($\text{NaAlSi}_3\text{O}_8$), the aqueous results underline a key point, namely
219 that Na, Al, and Si, and by analogy K, Al, and Si in a K-feldspar, can be considered to be mobile during
220 hydrothermal alteration at basic pH conditions.

221 A study of the Jurassic Navajo Sandstone by Zhu et al. (2006) revealed that SALs can also form
222 under natural conditions. TEM images show the presence of a naturally occurring 10 nm-thick
223 amorphous SAL that formed in situ on an alkali feldspar. The composition was not measured, but the
224 authors postulate that it is K-deficient and Si-enriched. Even though the formation fluid was found to be
225 mildly alkaline during borehole sampling, it is not known how the pH (and temperature) varied over
226 geological time. Quite importantly, this example shows that SALs are not ephemeral features of
227 dissolution, but can be stable over geologically long periods of time.

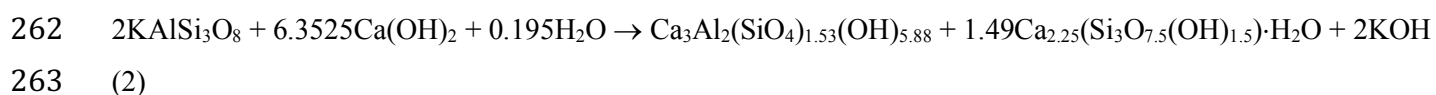
228 Over the past decade, there has been a resurgence of interest in the study of the chemical alteration
229 of K-feldspars. The objective of many recent studies has been to use very aggressive basic pH fluids to

230 chemically breakdown K-feldspars at hydrothermal conditions. The resulting secondary authigenic
231 phases that are produced during chemical alteration are enriched in K. This hydrothermal product can be
232 used directly as a K-fertilizer on soils, and is increasingly considered to be a commercially viable
233 substitute for traditional K-rich soluble salts, such as sylvite (KCl). Such soluble salts are nearly all
234 sourced in northern hemisphere countries (e.g., Belarus, Russia, Canada, Germany), making their long-
235 distance transport to developing countries in the southern hemisphere financially prohibitive. The
236 extraction of K-fertilizer from K-feldspars has a more than century-long history behind it, as described
237 in Ciceri et al. (2015). Despite this, little is known on the exact mechanism controlling this process. It is
238 interesting to note that over the past two decades several Chinese laboratories are spearheading this type
239 of research (see review in, e.g., Ma et al, 2015). In these Chinese studies (and others), the generalized
240 use of alkaline pH solutions to extract K is largely based on the economics of producing CaO from
241 limestone, from which Ca(OH)₂ is easily derived; there are also ‘green chemistry’ considerations that
242 come into play (Ma et al., 2015; Ciceri et al., 2017a).

243 Recent studies focused on the alkaline hydrothermal extraction of K from K-feldspars have for
244 the most part been centered on identifying and describing the secondary crystalline phases that are
245 produced. Moreover, although none has studied in detail the mechanism that controls the chemical
246 breakdown of the K-feldspar structure, a few have proposed scenarios on how this occurs. A study by Su
247 et al. (2015) reacted K-feldspar with aqueous KOH + NaOH solutions (8 M) at 240 and 280 °C, where
248 the mole fractions of KOH and NaOH were varied. These authors postulated congruent dissolution of
249 the feldspar via an OH⁻ mediated reaction:



251 The aqueous dissolution products on the right side of eqn. 1 consequently precipitate to form the
252 feldspathoidal mineral kalsilite, KAlSiO₄. When the above reaction is carried out with NaOH solvent,
253 sodium ions, in turn, reacting with Al(OH)₄⁻ and H₂SiO₄²⁻, lead to the precipitation of the feldspathoid
254 hydroxycancrinite, Na₈Al₆Si₆O₂₄(OH)₂·2H₂O. These crystalline phases formed as a dense amalgam of
255 crystals, which presumably precipitated directly from an oversaturated bulk fluid (see Fig. 2, Su et al.,
256 2015). The stoichiometric dissolution reaction detailed by Su et al. (2015) corresponds to the findings of
257 Gautier et al. (1994), who observed that Al and Si were released congruently from a K-rich feldspar at
258 150°C and pH 9.0. Another study, by Liu et al. (2015), hydrolyzed K-feldspar (microcline) in NaOH,
259 KOH, and Ca(OH)₂ solutions at hydrothermal temperatures up to 220 °C. They proposed a mineral-
260 mineral replacement process controlled by dissolution-precipitation, leading to the formation of hydrated
261 Ca-Al-silicate phases. At 220 °C they described the overall reaction as:



264 The above reaction, which proceeds via a transitional compound (not shown), results in the precipitation
265 of hydrogarnet and CSH phases (calcium-silicate-hydroxide). Even though the authors describe this as a
266 mineral-mineral replacement reaction, they did not present evidence for pseudomorphic replacement of
267 the feldspar, which is one of the defining characteristics of a true mineral-mineral replacement reaction
268 (see review in Putnis 2009, see also, e.g., Harlov et al. 2002; Putnis and Mezger 2004; Putnis et al. 2005;
269 Kasiopas et al. 2008). Thus, it would be more accurate to describe the overall reaction (Eq. 2) in terms
270 of congruent dissolution of the K-feldspar, followed by precipitation of secondary silicate phases from a
271 chemically saturated bulk solution. Other similar studies also support this type of process (Skorina and
272 Allanore 2015; Su et al. 2015; Liu et al. 2018, 2019).

273 A study by Ciceri et al. (2017a) used ultrapotassic syenite, an intrusive igneous rock with a very
274 high K-feldspar content, and poor in quartz. This material was subjected to 5 hours of alteration at 200
275 °C in a $\text{Ca}(\text{OH})_2$ solution. Based on chemical mapping and point analyses by electron probe
276 microanalysis (EPMA) of the reacted powder (thin section-mounted), Ciceri et al. (2017a) propose that
277 the original K-feldspar framework undergoes structural and chemical changes, and envision an OH-
278 mediated dissolution of the feldspar framework, accompanied by Ca-K exchange. They state that “no
279 single grain of K-feldspar preserved its original composition”, and go on to describe an amorphous
280 phase composed in part by “severely altered K-feldspar”. This terminology is rather ambiguous, in
281 particular as to whether such a phase, from a strict mineralogical-crystallographic point of view, can still
282 be considered to be a true feldspar. The invoked Ca-K exchange, however, falls within the framework of
283 traditional leached layer theory (Hellmann et al. 1990; Hellmann, 1999a,b, see also reviews and
284 references in Hellmann et al. 2003, 2012, 2015). In this case, interdiffusion ultimately controls
285 preferential loss of K^+ from the structure and concomitant replacement by Ca^{2+} from the solution. The
286 mechanism proposed by Ciceri et al. (2017a), however, can be questioned on a theoretical basis since it
287 involves an ultraslow process (i.e., solid-state diffusion at 200 °C) and an exchange couple (K^+ and
288 Ca^{2+}) involving cations with significantly different ionic radii and valence. These authors also propose
289 other possible mechanisms, including both mechanical and chemical, to explain Ca enrichment (see
290 electronic supplementary file, Ciceri et al., 2017a). A final comment concerns their use of EPMA.
291 Although this technique has superior detection limits compared to TEM-EDXS and EFTEM, it has a
292 much larger beam footprint, which means that the spatial resolution is not optimally suited for
293 determining the mechanism of dissolution.

294

295 **2 Material and methods**

296 **2.1 Sample preparation and characterization**

297 Five different orthoclase samples were collected from 2 outcrops of a late Jurassic porphyritic
298 felsite (an igneous rock with phenocrysts of orthoclase in a feldspathic matrix; also called orthophyre in
299 older literature) near the cities of Xinghe and Chifeng, Inner Mongolia, China. The geological ages and
300 emplacement histories of both felsites are very similar. These rocks were specifically chosen for their
301 high alkali feldspar content, which in turn, makes them interesting candidates for hydrothermal K-
302 extraction studies. This is the principal reason more common alkali feldspar-bearing rock types, like
303 granite, were not chosen for this study.

304 The samples were dry crushed and ground in an agate mortar. Orthoclase grains were isolated by
305 optical microscopy and heavy liquid separation, and then sieved, with the size fraction $< 74 \mu\text{m}$ being
306 used for the alteration experiments. The specific surface area of each powder was determined by N_2 -
307 BET analysis. Representative secondary electron SEM images of grains comprising the starting
308 materials (size fraction $< 74 \mu\text{m}$) for all 5 orthoclase samples are shown in the electronic Supplemental
309 Material appendix: Figs. S1a-e. As revealed by the SEM images, the large grains have a blocky
310 morphology, and show well developed cleavage planes. They do not appear to show any extensive
311 fracturing as a result of comminution. A few of the large grains have μm -sized internal void spaces, e.g.,
312 Fig. S1b. Based solely on an evaluation of the SEM images, these feldspars do not appear to have
313 undergone any seritization or argillization reactions. The distribution of grain sizes is very
314 heterogeneous, which is an expected finding for the preparation techniques used. No attempt was made
315 to remove the abundant surface fines created during mechanical diminution of the grains.

316 It is widely recognized that feldspar microstructures play an important role in chemical
317 weathering behavior and laboratory-measured dissolution rates. This has been documented for natural
318 and experimentally weathered alkali feldspars in studies by, e.g., Lee and Parsons, 1995; Lee et al.,
319 1998; see also references therein. The effect of microstructures on laboratory K-feldspar dissolution at
320 alkaline hydrothermal conditions has been reported by, e.g., Locati et al., 2010, and more recently in a
321 detailed study by Ciceri et al., 2017b. Dislocations and exsolution lamellae create localized regions of
322 higher strain, which cause these crystallographically perturbed areas to dissolve significantly faster than
323 the unstrained mineral structure. In this study, however, a detailed microstructural analysis of the raw
324 alkali feldspar samples was not an immediate goal, as we were not attempting to measure the kinetics of
325 dissolution, but rather the intrinsic mechanism of dissolution at the nanometer scale in interfacial areas
326 that were not affected by dislocations or exsolution lamellae.

327 Powder X-ray diffraction (XRD) confirmed that these 5 samples are orthoclase; the individual
328 diffraction patterns are shown in Fig. S2. In addition, XRD and Rietveld structure refinement were used
329 to determine semi-quantitative differences in Al/Si ordering. Diffraction patterns were collected using a
330 Pananalytical X'Pert Pro diffractometer using CuK α radiation at 40 kV and 40 mA, with a 0.0167° step
331 size over a 2 θ range of 10-90°. Rietveld structure refinements of the XRD patterns reveal that
332 differences in structural ordering (i.e., determined in terms of Al occupancy of t_1 tetrahedral site)
333 between the samples can be considered to be minor- an example of a Rietveld refinement of unaltered
334 orthoclase sample CHG-2- is shown in Fig. S3.

335 The mean chemical compositions and nominal chemical formulae of all 5 unaltered samples,
336 determined by X-ray fluorescence, are given in Table 1. A standard sample preparation protocol was
337 followed, and analyses were carried out using a Shimadzu 1500 XRF spectrometer. The compositional
338 analyses are based on 8 O atoms per formula unit, and the sum of the total cation charges (15.98-16.02)
339 equals the total anion charge based on O.

340

341 2.2 Hydrothermal alteration

342 The 5 orthoclase samples (Table 1) were reacted in separate experiments. This allowed us to
343 measure the physical, structural and chemical changes that characterize typical post-reaction feldspar-
344 fluid interfaces at the nm-scale on grains from each sample. We deemed that this approach might be
345 scientifically more interesting, as compared to running 5 replicates using just a single orthoclase sample.
346 The experimental protocol that we used here has been adapted from standard methods that have been
347 reported in other studies focused on the hydrothermal extraction of K from alkali feldspars in an alkaline
348 medium (Su et al, 2015; Liu et al., 2015; Ciceri et al., 2017a). The use of Ca(OH) $_2$ in this study as a base
349 was deliberate so as to avoid the common ion effect that would be associated with KOH, and to a lesser
350 extent, NaOH.

351 At the start of each experiment 1 g of orthoclase grains was mixed with 1 g of fresh CaO reagent,
352 after which 10 ml of ultrapure water were added. Given the hydrophilic nature of CaO, it is assumed that
353 an unknown amount of the oxide reacted with atmospheric humidity to yield Ca(OH) $_2$ during the setup
354 of each experiment. The pH $_{(25\text{ }^\circ\text{C})}$ of the starting solution before the orthoclase was added was 12.3-12.5.
355 The admixture was stirred for 5 minutes before being sealed in a 100 mL stainless steel autoclave with a
356 teflon liner. No degassing of the solution was carried out- therefore a non-quantified amount of
357 dissolved CO $_2$ was a component of the aqueous solution. The sealed autoclave was placed into an oven
358 pre-heated to 190 °C and left for 24 h at this temperature. The autoclave was then cooled down to
359 ambient temperature over a period of ~6 h, opened, and then heated again to 105 °C for 12 h in order to

360 drive off any remaining fluid. The retrieved solid cake was then reground by mortar and pestle to a size
361 fraction < 74 μm . The reground, altered material (hereafter ‘hydrothermal product’) served as the basis
362 for further solid-state analyses. The entire hydrothermal alteration process and the associated analyses
363 are schematically shown in Fig. 1. We note that one sample was reacted in duplicate, producing sample
364 CSY-1C-a. The experimental protocol was identical, except that the second heating step at 105 $^{\circ}\text{C}$ was
365 omitted since no liquid remained after the primary hydrothermal reaction step at 190 $^{\circ}\text{C}$.

366

367 **2.3 BET and XRD of reaction products**

368 The specific surface areas of the fresh and altered powders (< 74 μm size fraction) were
369 measured by N_2 -BET analyses using a Belsorp-Max volumetric gas sorption instrument. The samples
370 were first outgassed at 150 $^{\circ}\text{C}$ for 6 h under vacuum. The specific surface areas of powdered samples are
371 based on the Brunauer–Emmet–Teller (BET) equation ($0.05 \leq P/P_0 \leq 0.2$) using 16.2 \AA^2 as the cross-
372 sectional area of N_2 . The average surface area of the 4 starting materials is 3.4 m^2g^{-1} , while the altered
373 average is 12.6 m^2g^{-1} (Table 2). Thus, the average surface area increased by half an order of magnitude
374 due to alteration. As shown further on, the precipitation of an amalgam of very small secondary phases
375 explains this finding; this has also been confirmed in other similar studies. For example, using a particle
376 size distribution analysis of unreacted and reacted materials, Ciceri et al. (2017a- Fig. 6) noted a
377 significant shift to smaller particle sizes upon alteration, reflected both in terms of particle volume %
378 and particle number %.

379 Although the identification and detailed characterization of the crystalline authigenic phases
380 produced in the experiments were not the goal of this study, their presence cannot be neglected since
381 they occur within the interfacial region of the reacted feldspar grains, which was the main region of
382 interest. For this reason, we measured K concentrations associated with these secondary phases, as this
383 allowed us to qualitatively follow the fate of released K from the orthoclase. Below we describe the
384 standard X-ray powder diffraction (XRD) techniques that were employed to identify the crystalline
385 mineral phases present in the hydrothermal product- these are discussed further on in Section 3.1

386 The reacted samples were ground using a McCrone micronising mill to produce a size fraction <
387 1 μm . XRD analyses were run using a Bruker D5000 powder diffractometer equipped with a SolX Si
388 (Li) solid state detector (Baltic Scientific Instruments) using $\text{CuK}\alpha$ radiation at 40 kV and 40 mA.
389 Diffraction intensities were recorded at 0.026 $^{\circ}$ 2 θ -step intervals from 5 to 90 $^{\circ}$ (5 s counting time per
390 step) for bulk mineralogy determination. The identification of secondary mineral products by X-ray
391 diffraction (XRD) was based on matching the measured diffraction spectra with the ICDD powder

392 diffraction file database for phases that commonly occur when silicates are chemically altered at alkaline
393 hydrothermal conditions.

394 The Rietveld refinement method was then used to quantify the phases in terms of mass % (we
395 prefer this term vs. weight %). The generally accepted quantification limit is 1 mass %, although this can
396 be lower (~ 0.5) for phases with non-convoluted peaks. We used the code Profex (Döbelin and Kleeberg,
397 2015), which is a graphical user interface for Rietveld refinement of powder XRD data using the
398 program BGMN (Bergmann, 2005). In general, when the Rietveld refinement indicated that a selected
399 phase was present at < 1 mass %, this phase was then purposely deleted from further refinements- this
400 served to restrict the number of phases used for fitting.

401 The percentage of amorphous component in one sample (CSY-1C-a) was determined using a
402 standard method, Rietveld quantitative amorphous content analysis (de la Torre et al., 2001). This
403 method is based on measuring the XRD pattern of the hydrothermal product before and after the
404 addition of a known, precise quantity of an internal crystalline standard. While many standards can be
405 employed, we used pure corundum (Al_2O_3 ; Alfa Aesar, #42573 α phase). The sample-internal standard
406 mixture, containing exactly 30.4 mass % Al_2O_3 , was mixed and homogenized in the presence of ethanol
407 using a McCrone mill. As already noted above, sample CSY-1C-a underwent the same hydrothermal
408 alteration as CSY-1C, except that the heat treatment step at 105 °C was omitted. In general, XRD cannot
409 distinguish between a discrete amorphous phase and nano-crystalline or poorly crystalline material.
410 Therefore, the amorphous material quantified by XRD-Rietveld refinement in this study includes
411 discreet amorphous phases, as well as nanocrystalline and poorly crystalline material dispersed among
412 the secondary phases comprising the hydrothermal product.

413

414 **2.4 Resin impregnation**

415 After hydrothermal alteration the reacted orthoclase powders were embedded in a liquid C-based
416 epoxy resin (Struers) that was allowed to harden in a mold. The dried mounts were then polished on
417 SiC-coated disks in the presence of ultrapure water, finishing with a polish using a 5.0- μm
418 granulometry. This methodology provided us with embedded cross sections of randomly oriented
419 mineral grains and their alteration products. Even though brief contact with ultrapure water was
420 unavoidable during polishing, the resin impregnated the secondary products, thereby protecting them
421 from reaction with water. We also note that despite polishing, not all primary feldspar grains were flush
422 with the surfaces of the mounts. Numerous grains remained slightly below the polished surfaces, which
423 allowed secondary precipitated phases to be preserved in their native configuration on the grain surfaces.

424 For example, in Fig. 2b, note the presence of ‘free standing’ scalenohedral calcite crystals on top of the
425 orthoclase grain. The lack of any visible signs of chemical corrosion, in particular with respect to soluble
426 secondary phases like calcite, support the premise that the protocol we used was not deleterious. The
427 remaining primary K-feldspar grains also did not display any evidence of additional dissolution (e.g.
428 etch pits) from the polishing step. This is perhaps expected, as feldspars in general are quite robust
429 minerals, and are not very reactive in pure water at ambient temperature. All samples were carbon
430 sputter coated before analysis by FESEM (C-coat thickness was a few tens of nm).

431

432 **2.5 FESEM**

433 Even though the main analytical technique for this study was TEM, we also used scanning
434 electron microscopy (SEM) to obtain images at the μm -scale. This allowed us to obtain an overall large-
435 scale picture of the nature of the reacted feldspar grains. The secondary precipitates form a ‘reaction
436 rim’ around each grain. Because the objective of our study was a detailed investigation of the orthoclase-
437 fluid interface, we deemed it logical to also include these secondary precipitates in our measurements
438 and observations at both the μm and nm scales.

439 The polished mounts from all 5 experiments were extensively investigated. Individual orthoclase
440 grains and their rims of hydrothermally altered products were imaged with a high-resolution field
441 emission scanning electron microscope (FESEM): Zeiss Ultra Plus (PISA Facility- GFZ Potsdam). The
442 acceleration voltage was 20 kV, with a 120- μm aperture. The use of standard detectors allowed imaging
443 of backscattered (BSE) and secondary electrons (SE). Chemical maps and spectra were measured by
444 energy dispersive X-ray spectroscopy (EDXS). The FESEM is equipped with a Thermo Fisher Scientific
445 UltraDry SDD EDX detector. The chemical spectra are based on standard *K*-lines for all elements of
446 interest (Si, Al, O, K, Na, Ca, C). We examined the orthoclase samples by FESEM imagery, EDXS spot
447 analyses (ZAF-corrected), and chemical maps (based on raw net counts with background subtraction).
448 The ZAF-corrected elemental counts can be considered to be semi-quantitative. Analyses of carbon in
449 particular are problematical because of the unavoidable contributions from the epoxy resin to the total C
450 signal, and to a much lesser extent, from the carbon sputter coating. This resulted in probable
451 overestimations of C in carbon-bearing secondary phases, in particular calcite that precipitated within
452 the amalgam of secondary phases.

453

454 **2.6 FIB**

455 Using focused ion beam (FIB) preparation, electron transparent ultra-thin sections were extracted
456 from selected grains embedded in polished sections. Two samples of resin-embedded altered orthoclase

457 (CSY-1C and CSY-3C) were investigated at the nanometer-scale by TEM. With respect to sample CSY-
458 1C, two FIB lamellae were fabricated at different locations on the same grain that was previously
459 observed by FESEM. For CSY-3C, one FIB lamella was produced from a grain that had also been
460 investigated by FESEM. The FIB thin sections were prepared with a FEI Helios G4 UC Dual Beam
461 (SEM-FIB) instrument housed at GFZ. In general, the FIB lamellae were milled from vertical cuts on
462 polished grain surfaces. For each lamella, a large primary orthoclase grain was selected, and the milling
463 location was chosen so as to include the interface between the grain and the adjacent lateral alteration
464 rind composed of secondary precipitates.

465 The FIB protocol can be very briefly summarized as follows. After the deposition of a Pt strap at
466 the chosen area on a polished grain surface, milling with a Ga beam proceeds at an accelerating voltage
467 of 30 kV and a beam current of 47 nA, which is later on decreased to 9 nA. After the lamella is cut free
468 from the matrix, it is transferred in situ to a Cu TEM grid, where it is welded to one of the grid posts.
469 Once firmly attached, additional thinning takes place with a 30 kV, 41 pA Ga beam. Progressive
470 thinning is achieved by steadily decreasing the voltage, such that in the final step, the voltage is reduced
471 to 5 kV. The final step ensures that much of the lateral-edge amorphous material created during milling
472 is effectively removed. The final result is an electron transparent ultrathin section with typical
473 dimensions of 15-20 μm (length) x 5-10 μm (height) x 150-200 nm (thickness). A more detailed
474 description of the procedure that we used can be found in Wirth (2009). Even though not available to us
475 at the time, as a final step it is generally advisable to remove implanted Ga from FIB lamellae using an
476 Ar ion nano-milling technique (see, e.g., Supplemental Information in Leonard and Hellmann, 2017).

477

478 **2.7.1 TEM: FEI Tecnai**

479 The vast majority of the transmission electron microscopy work was carried out on a FEI Tecnai G2
480 F20 X-twin FEG TEM operating at 200 kV (GFZ). This TEM is equipped with standard BF (bright
481 field), DF (dark field) and STEM-HAADF (scanning TEM-high angle annular dark field) detectors, a
482 post-column Gatan Tridiem energy analyzer for EFTEM (energy filtered TEM) and EELS (electron
483 energy-loss spectroscopy), and an EDAX energy dispersive X-ray spectrometer equipped with a Si-Li
484 detector. We did not attempt to determine complete chemical compositions at specific locations by
485 EDXS spot analyses- this normally requires separate analysis of external standards. Instead, we scanned
486 the electron beam within a pre-selected area (whose size was dependent on the object being analyzed),
487 and then quantified the chemistry using three elemental atomic ratios: Al/Si, K/Si, and Ca/Si (Table 3).
488 As a first approximation, we assumed that the ‘thin-film’ criterion holds, which means that X-ray
489 absorbance and secondary fluorescence effects are ignored. The Cliff-Lorimer method (Cliff and

490 Lorimer, 1975), based on k_{AB} factors, was used to determine atom % of Al, Si, K, and Ca, allowing
491 Al/Si, K/Si, and Ca/Si ratios to be determined. For these elements, the built-in EDAX software
492 standardless k_{AB} factors were considered to be sufficiently accurate; however, this was not true for O.
493 Due to Ga implantation into the lamella during the FIB fabrication process, we did not attempt to
494 quantify Na by deconvoluting overlapping Ga *L* and Na *K* peaks in EDXS spectra.

495 In several instances, we recorded selected area EELS spectra of the C *K* and the Ca *L*_{2,3} edges (in
496 EELS spectrum mode) of prominent bands that parallel the orthoclase interface. In each case, the EELS
497 background was fit with a standard polynomial function and subtracted from the spectrum using a
498 standard method that is a part of the Gatan® GMS software package. In addition to EELS, we also used
499 EFTEM to provide relatively high spatial resolution chemical maps of certain interfacial regions.
500 EFTEM is an advanced method for obtaining chemical maps of light elements with nanometer-scale
501 spatial resolution (Grogger et al., 2003). The detection limit is generally in the parts per thousand range.
502 The distribution of a chosen element can be portrayed either with a 2-window (jump ratio) or a 3-
503 window (chemical map) image. To produce a jump ratio image of a certain element, an appropriate
504 ionization edge is chosen, and two energy-filtered images are made, one before the edge, and one after.
505 The post ionization edge image is then divided by the pre-edge image, and the result is a jump ratio
506 element distribution map. The 3-window map approach is based on obtaining two pre-edge images and
507 one post edge image. The spectral background curve is then calculated, such that the area under the post-
508 edge peak can be determined- this difference is the net core-loss signal, which is proportional to the
509 concentration of the element.

510

511 **2.7.2 TEM: FEI Themis Titan**

512 The second TEM instrument that we used is a recent aberration-corrected FEI Themis Titan that
513 was operated at 200 kV (Minatec, Grenoble, France). This TEM, with its four Bruker EDX detectors (30
514 mm² x 4; 0.68 radians), allows for very rapid acquisition of chemical maps with much lower beam
515 currents compared to conventional TEM instruments (e.g., Tecnai, GFZ). We typically used beam
516 currents of 200 pA. Because of these technical advantages, this TEM instrument was principally used to
517 obtain high-resolution STEM and EDXS chemical maps of the interfacial regions. Measurements of
518 certain elements, such as K and Na, on the same feldspar interfacial areas with both TEM instruments
519 revealed the inherent advantages of the FEI Themis. It has already been reported that the measurement
520 of accurate K and Na levels in silicates by analytical TEM is difficult due their mobility under an
521 electron beam (van der Pluijm et al., 1988). This phenomenon is particularly prevalent in thinner areas
522 near grain edges. Factors such as probe size and current, sample thickness, and crystallographic

523 orientation have been shown to play important roles. In addition to these factors, the position of the
524 detector with regard to a wedge-shaped sample (most FIB thin foils are in fact wedge-shaped in cross
525 section) directly affects the X-ray absorption distance (Williams and Carter, 2009), which can also
526 influence the EDXS measurements.

527 The EDXS chemical maps were generated by X-ray intensities measured by the 4 EDX detectors,
528 and are based on measured elemental *K* edge intensities that have not been corrected. Thus, EDXS maps
529 show relative concentrations for each element. On the other hand, quantitative chemical analyses of
530 specific areas were measured with just one of the four detectors, as we selected the detector that offered
531 the best detector-sample geometry in order to reduce as much as possible X-ray absorption effects.
532 Moreover, specific-area chemical compositions have been corrected for X-ray absorption effects
533 according to the iterative ζ (zeta) method described by Watanabe and Williams (Williams and Carter,
534 2009; Watanabe and Williams, 2006) and implemented using a specific code (Robin, 2017). This
535 method largely surpasses the Cliff-Lorimer (i.e. *k* factor correction) method (Cliff and Lorimer, 1975)
536 and provides a relatively accurate quantification of the chemical composition.

537

538 **3. Results**

539 **3.1 X-ray powder diffraction and Rietveld refinements.**

540 X-ray powder diffraction (XRD) of the five original hydrothermally altered orthoclase samples
541 was used to identify the major (> 0.5 mass %) crystalline phases, followed by Rietveld refinements
542 (Figs. S4a-e) to estimate the approximate mass percentages present. One additional sample, the replicate
543 CSY-1C-a, was similarly analyzed (Fig. S4f). All six diffraction diagrams show a strong central peak
544 (calcite), in conjunction with other distinct smaller peaks and numerous very weak peaks. Fitted
545 backgrounds (Figs. S4a-e) reveal a smooth bump between 20-50° (Cu *K* 2 θ), suggesting roughly similar
546 amounts of amorphous material in all 5 samples. The replicate sample (CSY-1C-a, Fig. S4f) was
547 analyzed specifically for its amorphous content, which was determined to be ~16 %. This compares to
548 amorphous components of 18 % (Ciceri et al., 2017a) and 5-30 % (Liu et al., 2019) reported in other
549 studies devoted to alkaline hydrothermal alteration of K-feldspars.

550 XRD confirms that the conversion of orthoclase did not go to completion in the hydrothermal runs,
551 as the fraction of unaltered orthoclase is significant, 11-21 %. No other feldspar phases were found (>
552 0.5 mass %), in particular potential secondary authigenic feldspars. In all experiments, the dominant
553 secondary phase that formed is calcite (CaCO₃), 35-50 %. A minor amount of the polymorph vaterite
554 formed in only one experiment, CSY-1C-a (1.5 %). Since the orthoclase samples contain only trace

555 amounts of Ca (Table 1), calcite is rather a byproduct of aqueous calcium cations reacting with dissolved
556 atmospheric CO₂ in the CaO-H₂O alkaline solvent, and then precipitating during the course of the
557 experiments.

558 After calcite, the next most abundant secondary phases are all silicate minerals containing variable
559 amounts of Ca and Al oxides, and including OH and/or H₂O. Crystalline phases with these chemical
560 components also commonly form during cement hydration experiments, which is logical, as alkaline
561 conditions are also prevalent. We thus make use of the CASH and CSH nomenclature from the cement
562 literature to designate in a generalized manner non-stoichiometric calcium (CaO)-aluminate (Al₂O₃)-
563 silicate (SiO₂) hydrate (OH, H₂O) mineral phases. As described later on, the secondary products that
564 formed are for the most part an amalgam of intergrown and superposed phases, and thus we simply refer
565 to them together as CASH, CSH, and/or carbonate.

566 The sum of CASH and CSH phases make up between 43.0 and 54.3 % of the final run products,
567 with one outlier (sample CHG-12C) at only 28.4 %. The two replicate experiments (CSY-1C and CSY-
568 1C-a) have very similar values, 52.9 and 52.8 %. Equation 2 describes a possible macroscopic reaction
569 for the formation of these secondary silicate phases. The two most prominent CASH minerals (18-24 %)
570 are the cubic phases hibschite and katoite. Both are hydrated members of the (hydro)grossular garnet
571 series (see note S1): Ca₃Al₂(SiO₄)_{3-x}(OH)_{4x}: grossular, $x = 0$; hibschite, $x = 0.2-1.5$; katoite, $x = 1.5-3.0$
572 (with increasing hydration OH substitutes for SiO₄ groups). The dominant CSH mineral that precipitated
573 is tobermorite 11 Å (8-31%), which crystallizes in the orthorhombic system with a fibrous or bladed
574 habit: Ca₅Si₆O₁₆(OH)₂·4H₂O. Coupled substitution of [Al³⁺ + Na⁺] for Si⁴⁺ can result in an Al-substituted
575 11 Å tobermorite. Fitting the tobermorite peak proved to be the most challenging aspect of the Rietveld
576 refinements, and was achieved with an adjustable mixture of micro- and nano-crystalline crystals. Using
577 the Bragg equation we verified that the *d*-spacing was indeed 11 Å for this phase.

578 During the Rietveld refinements, in order to constrain our results to the major secondary phases
579 present, we purposely excluded phases with concentrations less than 1 mass %. However, this
580 discrimination protocol doesn't imply that these phases did not form, but simply that they precipitated
581 very sparingly, and it was decided not to quantify them further. Thus, the crystalline phases vaterite
582 (CaCO₃), bütschliite (K₂Ca(CO₃)₂), α-dicalcium silicate hydrate (Ca₂SiO₃(OH)₂), kalsilite (KAlSiO₄),
583 hydroxycancrinite (Na₈Al₆Si₆O₂₄(OH)_{1.4}(CO₃)_{0.3}·6.35(H₂O)), belite (Ca₂SiO₄), and panunzite
584 ((K,Na)AlSiO₄) were excluded from our final results (excepting vaterite in CSY-1C-a). Figure S5 shows
585 the partitioning of the hydrothermal product from the 6 alteration experiments in terms of remaining
586 orthoclase and the major secondary crystalline phases.

587 In a broad sense, the secondary phases determined in our study are similar to those in other studies
588 that have focused on alkaline hydrothermal extraction of K from alkali feldspars. It is important to note
589 that the exact assemblage of secondary mineral and amorphous phases depends on many variables, and
590 can be a function of different starting materials (alkali feldspar-rich rock vs. alkali feldspar), different
591 polymorphs of alkali feldspar, differences in internal microstructures and Al/Si ordering, solvents with
592 different chemical compositions, i.e., NaOH, KOH, Ca(OH)₂, and differences in temperature, run times,
593 water/rock ratios, as well as other experimental variables. Overall, hydrogrossular and tobermorite have
594 been reported to be generally present in other studies, but their proportions are quite variable (Liu et al.,
595 2015, 2018, 2019; Ciceri et al., 2017a). Abundant calcite was also measured in studies by Liu et al.,
596 2015, 2018, 2019. Phases such as α -dicalcium silicate hydrate and panunzite have been documented, but
597 in higher proportions than in our study (Ciceri et al., 2017a; Liu et al., 2018, 2019). Moreover, some
598 studies have found a much different assemblage of secondary minerals (e.g., Su et al., 2015), dominated
599 by kalsilite and hydroxycancrinite, for example. One study has listed as the dominant hydrothermal
600 product phase ‘altered’ K-feldspar (66.5 %, Fig. 2, Ciceri et al., 2017a), but as already discussed, the
601 meaning of what this ‘phase’ actually represents is not clear.

602

603 **3.2 Micrometer-scale images by FESEM and EDXS.**

604 Numerous altered orthoclase grains from all 5 samples were examined in polished cross sections at
605 various scales by field emission scanning electron microscopy (FESEM) and energy dispersive X-ray
606 spectroscopy (EDXS). Here we describe one representative sample: CSY-1C. Figure 2a is a secondary
607 electron (SE) image of a large primary grain of orthoclase characterized by a prominent 1-2 μm -thick
608 halo of secondary precipitated phases. This type of morphology characterizes orthoclase grains in all
609 samples. The rind of secondary phases (Fig. 2b, location 1) contains both fine-grained material and
610 larger bladed precipitates (probably tobermorite, with some calcite; calcite also formed individual μm -
611 sized scalenohedral and rhombohedral crystals on the polished surface). The three globular entities
612 above the large grain (nos. 2, 3, 4) are estimated to be an amalgam of CASH + CSH phases and calcite,
613 with variable amounts of small orthoclase grains.

614 The EDXS chemical maps in Fig. 3a-f show the relative concentrations of K, Ca, Si, Al, C, and O at
615 the same grain location (Fig. 2b). Compared to the uniformly high concentration of K in the large
616 orthoclase grain, K is present at significantly lower levels in the alteration halo (rind, no. 1) and in the
617 large globular entity (no. 4), but at relatively higher levels in entity 2, and particular in entity 3.
618 Potassium at locations 1-4 is associated primarily with secondary phases, and to a lesser degree with
619 very small orthoclase grains. The rind (area 1) is particularly enriched in Ca, but nonetheless, also

620 contains Si, Al and O at lesser concentrations. It most likely consists of a mixture of calcite and CASH +
621 CSH phases. Entities 2 and 3 show a relatively good correlation among K, Ca, Si and Al. In contrast,
622 entity 4 is different: enrichment in Ca and O, low Si, and near absence in Al. Aside from a notable C
623 presence in the resin, there are a few C hotspots present in the rind (no. 1), with lesser amounts visible in
624 entities 3 and 4, and the periphery of entity 2 (but lacking in core). The partitioning of the total carbon
625 signal, while heavily weighted to the resin, is of course also attributable to CaCO_3 (calcite) precipitates.
626 Even though one would expect a good spatial correspondence between C and Ca, this is not always the
627 case, e.g., in the rind (1). Binary elemental overlay maps (Figs. S6a-c) reinforce the conclusions drawn
628 from the single element maps.

629 630 **3.3 Nanometer-scale measurements of orthoclase interface by TEM.**

631 **3.3.1 Chemistry and structure of feldspar and precipitates**

632 Figure 4a is a HAADF-STEM image of an orthoclase grain (CSY-1C) prepared in cross section by
633 focused ion beam milling (FIB). The white arrows indicate a sharp and distinct interface between the
634 orthoclase and the enveloping alteration halo of secondary precipitates. The precipitates display various
635 types of morphologies, including a single large grain, granular aggregates, bladed crystals, and a
636 probable amorphous phase characterized by a large (~400 nm) pore, abutting the orthoclase grain. The
637 majority of the material in the alteration halo is slightly darker in tone, indicating lesser mass-density
638 compared to the orthoclase. The 8 rectangles indicate the areas that were analyzed by EDXS (Table 3).

639 Areas 1 and 2 correspond to the nominal composition of orthoclase, with the expected atomic
640 ratios; e.g., $\text{K/Si} = 0.24$ and 0.23 at locations 1 and 2, respectively. In other grain interior locations of
641 this sample, similar K/Si values were recorded, resulting in an average nominal orthoclase K/Si ratio of
642 0.24 - 0.25 . Curiously, at area 3, which is at the edge of the orthoclase grain, the K/Si ratio is only 0.17 ,
643 which is significantly lower than the nominal value, and yet the measurement was taken fully within
644 orthoclase. This was found to be the case with many other (but not all) EDXS measurements taken at
645 grain edges, where in some cases, K/Si values are even lower. As detailed further on, this effect is not
646 due to chemical alteration and leaching of K from the orthoclase, but is rather an analytical artifact. The
647 Ca/Si ratios measured at areas 1-3 reveal that at the scale of the analyses and the analytical resolution of
648 these particular TEM-EDXS measurements, there is no evidence for Ca entering into the orthoclase
649 structure. Based on morphology and chemical composition, areas 6 and 8 most likely correspond to an
650 amalgam of hydrogrossular and tobermorite phases. The phases represented by areas 4, 5, and 7 are
651 difficult to identify, but based on chemistry and morphology, 7 may be Al-tobermorite. The large pore
652 and low mass-density suggest that area 4 is amorphous. This area is located in what appears to be a

653 discreet phase with low mass-density that directly abuts the orthoclase edge. Area 5 has elevated K/Si
654 and Al/Si ratios, and a Ca/Si ratio indicating minor Ca enrichment- this phase is not identifiable,
655 however. Notwithstanding the tenuous identification of the secondary phases, they all contain K, and in
656 one case (area 5), a K/Si value of 0.30 is measured (i.e., compare to nominal unaltered orthoclase value
657 of 0.22).

658 The HAADF-STEM image in Fig. 4b shows a cross-sectional view of a primary orthoclase grain
659 (CSY-3C), also with a sharp boundary between orthoclase and secondary precipitates. Four areas were
660 measured by EDXS analyses (Table 3). The chemistry of area 9 has elevated K levels, and may
661 represent a mixture of Al-tobermorite with other phases (i.e. measured Ca/Si = 1.11). Area 10 is likely a
662 resin-filled pore primarily composed of C and O, but K, Ca, Al, Si are measurable in the spectra, which
663 is possibly attributable to the presence of nano-precipitates that are not visible in the image. The
664 presence of a 60-nm thick continuous band of precipitate in close proximity to the orthoclase sets this
665 image apart from previous examples. The EDXS spectrum reveals (area 11) a very high Ca
666 concentration, significant C, the near absence of Si and Al, and elevated K- it is therefore most likely
667 calcite, but in the presence of a minor phase(s) containing K. We can at this point only speculate that the
668 elevated K concentrations might be due to the presence of K-bearing nanoparticles, or possibly even a
669 K-rich carbonate phase, such as K_2CO_3 (formed via one possible reaction: $KOH + CO_2_{aq}$), or even
670 bütschliite, $K_2Ca(CO_3)_2$. The chemical analyses at area 12 correspond to the composition of unaltered
671 orthoclase, with K/Si = 0.23. Calcium is present at the EDXS detection limit, Ca/Si = 0.0011.

672 A second HAADF-STEM image of the same interface (CSY-3C), but at a new location, is shown in
673 Fig. 4c (EDXS chemistry of areas 13-16, see Table 3). The band of calcite, while not well defined, is
674 still present, with K/Si = 0.09 (area 14). As already discussed, the measured K and Si most likely
675 indicate the presence of minor amounts of silicate particles. Here the band is separated from the
676 orthoclase by a precipitate (area 13) with pores having dimensions of several tens of nm (pores appear as
677 black entities). The presence of numerous pores and the general morphology, the low mass-density, and
678 a chemical composition inconsistent with any of the phases identified by XRD (Fig. 2), suggest that this
679 may be an amorphous phase, perhaps similar to the one described in Fig. 4a. Areas 15 and 16 have
680 relatively similar Al/Si and Ca/Si chemistries, and may be an amalgam of crystalline and amorphous
681 material. Their K/Si ratios are very different, however, which at area 15 is 0.60. This elevated ratio
682 cannot be attributed to a very low concentration of Si, given that the Si counts are the same in area 16.
683 Whether there is any calcite in this region is not known. Figure 4c also shows the omnipresence of
684 white-colored nm-sized precipitates. Further along the same interface, 4 more areas were characterized
685 (areas 17-20, Table 3; TEM image in Fig. S7). Area 17, which is within another thin band of (possibly

686 amorphous) precipitate in close proximity to the orthoclase, also has an elevated K/Si ratio = 0.19.
687 Taken together (Figs. 4a-c, Fig. S7), these findings reveal that certain secondary phases, both crystalline
688 and amorphous, are associated with significant levels of K.

689

690 **3.3.2 Calcite in interfacial region**

691 The intermediate resolution bright field (BF) TEM image in Fig. 5a (CSY-3C) displays another
692 example of a continuous ~60 nm-wide linear band of calcite that runs parallel to the orthoclase interface.
693 In BF imaging, calcite is easily distinguished by its mottled appearance. The calcite band does not touch
694 the orthoclase, but rather occurs within an aggregate of precipitated phases characterized by bladed
695 crystals (likely tobermorite), a large granular globule (demarcated by 3 open-ended arrows), and a fine-
696 grained matrix between the bladed crystals. The matrix itself contains nm-sized dark grains, which
697 probably correspond to the white grains observed in Fig. 4c. The presence of numerous bubbles (e.g.,
698 white globules, next to scale bar) throughout the precipitate most probably indicate trapped water, which
699 would imply that the precipitation rind is significantly hydrated. The external edge of the orthoclase
700 grain appears to end abruptly at a continuous parallel band that may be amorphous (2 white arrows,
701 dashed tails).

702 To confirm the presence of calcite in the aforementioned bands (Figs. 4b,c, 5a), we recorded
703 selected area EELS spectra of the C *K* and the Ca *L*_{2,3} edges (in EELS spectrum mode). The
704 deconvolved, background subtracted spectrum (Fig. 5b) of the band delimited by the solid white arrows
705 in Fig. 5a confirms that this is calcite. The spectra show two distinct C *K*-edges, one at 289 eV and the
706 other at 300 eV. These two edges are characteristic for calcium carbonates, and represent two different
707 electronic transitions, the first 1s/π* (C=O) and the second 1s/σ* (C-O) (Martin et al., 1996). The peak
708 maxima for the Ca *L*_{2,3} peak are at 348 and 351 eV. The C and Ca spectra provide proof that the uniform
709 and continuous bands, as evidenced in Figs. 4b,c and 5a, are crystalline Ca-carbonates. Based on the
710 EELS spectra alone, it is not possible to distinguish between the two polymorphs calcite and vaterite, but
711 the Rietveld refinement for this sample favor the former.

712

713 **3.3.3 Does Ca enter the orthoclase structure?**

714 To determine the chemical stability of the original orthoclase structure with respect to the Ca-rich
715 solvent during the alteration process, we investigated whether there was evidence for Ca entering the
716 orthoclase structure by interdiffusion, or alternatively, by the replacement of the original orthoclase with
717 a Ca-rich secondary phase, such as anorthite, the Ca-end member plagioclase feldspar (CaAl₂Si₂O₈). To

718 explore this question we used energy filtered TEM (EFTEM) imaging, a powerful and yet under-utilized
719 TEM method in mineralogy and geochemistry. Figures 6a, b are complementary images, and both show
720 the same well-defined interface (white arrows) between orthoclase (CSY-1C) and secondary
721 precipitates. The first is a BF TEM image- it shows a complex amalgam of secondary precipitates,
722 including bladed crystals, a fine-grained grey groundmass, calcite (?), nanometer-sized particles, and
723 what appear to be extremely small globules (light grey to white, indicating possible evidence for water).
724 The precipitates terminate abruptly at the orthoclase interface.

725 Figure 6b is the corresponding Ca $L_{2,3}$ EFTEM 3-window chemical map at slightly lower
726 magnification. The widths of the 3 windows (all equal in energy) and the polynomial function used to fit
727 the spectral background were calculated with Gatan Microscopy Suite (GMS) software. In the Ca map,
728 white regions correspond to elevated Ca concentrations (secondary precipitates), and conversely, black
729 regions indicate a lack of Ca, such as is the case for the Ca-devoid orthoclase structure and resin. Note
730 that the precipitates do not have a uniform white color, which indicates variable Ca levels and/or
731 differences in thickness. Most importantly, the chemical gradient of Ca at the orthoclase-precipitate
732 interface is quite sharp and resembles a step-function change. Therefore, at the spatial/energy resolution
733 of this EFTEM image, there is no evidence for the incorporation of Ca into the orthoclase structure,
734 either by mineral-mineral replacement or by interdiffusion.

735 The interested reader may question why a potassium EFTEM chemical map is not shown, in
736 particular since K is a good tracer for chemical alteration of the orthoclase structure. The omnipresence
737 of carbon, which makes up the resin, makes this technically very difficult because the K $L_{2,3}$ and the C K
738 ionization edges are nearly at the same energy. Deconvoluting the K and C EEL spectral signatures is
739 technically very difficult, and thus was not attempted. The other major K absorption edges could
740 theoretically be used, but they occur at either too high (K edge at 3607 eV) or too low energy ($M_{2,3}$ edges
741 at 18 eV), such that in practice it would be difficult to extract a quantitative signal to calculate an image.

742

743 **3.3.4 Advanced STEM-EDX: the effect of electron dose**

744 The K/Si values measured in areas 1-3 in Fig. 4a bring up an important point, as K/Si ratios were
745 often anonymously low at orthoclase grain edges when compared to regions a few hundreds of nm
746 towards the interior of the grain. These elemental concentrations were measured with the Tecnai TEM
747 using a 1 nA probe current (24.9° sample tilt). We therefore proceeded to investigate this in more detail
748 by measuring K/Si values at another close by area on the same orthoclase grain edge with an advanced
749 analytical TEM, the aberration corrected Titan Themis (Minatec). For these measurements we used a
750 significantly smaller probe current of just 200 pA (0° tilt). Numerous measurements close and directly at

751 the interface confirmed that nominal, unaltered orthoclase K/Si values were obtained. Thus, the low K/Si
752 values described above (section 3.3.1, Fig. 4a) are clearly an analytical artifact. This example illustrates
753 the advantages of using a 4-detector EDXS system that allows for very fast X-ray acquisition times
754 using very low beam currents. These results also point out that orthoclase grain edges, perhaps due to a
755 thickness effect, are more prone to alkali diffusion than grain interiors, in particular when too high beam
756 currents are used, or if the acquisition time is too long (refer also to study by van der Pluijm et al., 1988).

757 Going further, to quantify the importance of the electron dose on K and Na measurements, we
758 measured the EDXS counts of K, Na, Al, and Si on several consecutive, same-sized areas of orthoclase
759 sample CSY-1C as a function of the total electron dose. The measurements were made towards the
760 interior of the grain, and away from the edge. The dose is defined as the number of electrons that
761 impinge upon 1 nm² of surface, and is expressed in units of pA·s·nm⁻². Figure 7 schematically shows the
762 evolution of the stoichiometrically normalized elemental ratios, expressed in terms of Si/3Al,
763 (K+Na)/Al, K/Al, and Na/K. All of the ratios are fitted to discrete linear trends over the entire range of
764 electron doses probed. The linear and constant trend defining Si/3Al indicates that Si and Al are not
765 affected by electron doses inferior to 0.7 pA·s·nm⁻². The Na/Al trend can be interpreted in terms of a
766 very slight loss of Na with increasing dose in the ‘K, Na loss region’ of Fig. 7. On the other hand, the
767 K/Al and (K+ Na)/Al intensities appear to be roughly constant in the low dose region (< 0.15 pA·s·nm⁻²
768 ²), but then show a marked linear decrease at higher doses. These results, somewhat surprisingly,
769 indicate that K is much more susceptible to electron dose-induced thermal diffusion compared to Na.
770 Overall, the relations shown in Fig. 7 indicate that TEM-EDX measurements are best done in the ‘no
771 loss’ region corresponding to a total dose < 0.15 pA·s·nm⁻², in particular for measurements at thinner
772 edge regions. Taken together, these results confirm that the anomalously low K/Si values often
773 measured in areas close to K-feldspar grain edges are most likely due to too high electron doses (e.g.,
774 area 3, Fig. 4a).

775

776 3.3.5 Advanced STEM-HAADF-EDXS measurements of an interfacial SAL

777 Using the Themis TEM, we obtained a moderate-resolution STEM-HAADF image of an interfacial
778 region on orthoclase grain CSY-1C (Fig. 8). The vertical dashed line delimits the interface between the
779 orthoclase and a presumably amorphous surface layer (SAL). A relative thickness profile on the STEM-
780 HAADF image, generated by iterative calculations using elemental X-ray intensities (Robin, 2017),
781 reveals that the orthoclase edge region is thinner than the bulk material further away. There are also
782 slight inhomogeneities in the grey tone of the orthoclase: a. the bottom half of the unaltered orthoclase

783 region appears slightly lighter in color, b. numerous small white flecks are present on the orthoclase
784 surface, particularly evident on the right side of Fig. 8a. These inhomogeneities are probably due to
785 minor redeposition (sputtering) of the adjacent amorphous material (SAL) that occurred either during
786 FIB milling, or EDXS analyses. The amorphous material is probably composed of a ‘soft’ gel-like
787 material that is easily prone to electron or ion beam sputtering.

788 Figure 8 also shows normalized chemical profiles that were determined along the same trace used
789 for the thickness profile. The K/Al profile is characterized by a nm-sharp, step function-like jump at the
790 interface between the orthoclase grain edge and the abutting amorphous phase. The behavior of the K/Al
791 ratio as it transitions from orthoclase to the amorphous phase (SAL) is due to the combined effects of a
792 sharp increase in K concentrations and a concomitant decrease in Al. In contrast, the Na/Al ratio remains
793 roughly constant in both phases. The profile of Si/3Al is relatively constant, with a value near 1.0 within
794 the orthoclase. As the profile passes into the SAL, the ratio exhibits more variability, but remains close
795 to an average of 1.0 over a distance of 0 to -30 nm. At distances < -30 nm the ratio shows a monotonic
796 but fluctuating increase to a value of ~1.7. The fluctuations may be due to pores or other
797 inhomogeneities in the SAL. The O/8Al profile displays virtually identical behavior to the Si/3Al profile
798 in the orthoclase and over 0-30 nm within the SAL. However, at distances < -30 nm in the SAL, the
799 O/8Al profile surpasses the Si/3Al profile. One interpretation for O/8Al > 1 is the presence of H₂O,
800 indicating hydration of the SAL. The largest positive spikes in the O/8Al profile may in fact correspond
801 to water inclusions. Even without a statistical analysis, there is a surprising correlation between many of
802 the Si/3Al and O/8Al profile peaks in the SAL. One final note concerning the potential redeposition of
803 amorphous material onto the orthoclase surface; there is no effect on the Na/Al, Si/3Al, and O/8Al
804 profiles, and only a very insignificant effect on the K/Al profile within the orthoclase.

805 The STEM-HAADF image in Fig. 9a is derived from a cropping of Fig. 8a, thereby allowing
806 additional details of the interface to be more clearly shown. This image clearly shows a prominent and
807 sharp vertical interface (white arrows) that marks a sudden transition in both structure and chemistry,
808 which is manifested by a difference in mass-density between the orthoclase (right) and an amorphous
809 SAL (left) with lower mass-density. The even less dense large pores appear black, in particular the
810 bottom most one. The presence of such large pores can be construed as indirect evidence for the
811 amorphous nature of the SAL- note also their morphological resemblance to those in Fig. 4a-c. The
812 origin of the thin vertical band that appears at the external edge region of the orthoclase is not
813 understood, but it may be an artifact.

814 Figure 9b is a superposition of K, Ca, and Si EDXS maps onto the STEM-HAADF image, after a
815 ‘smooth’ filter was applied. The corresponding individual elemental (Ca, K, Al, Si) EDXS maps, which

816 have also been superposed on the same STEM-HAADF image, are shown in Fig. 9c. The individual
817 concentrations (i.e. colors) in the latter maps are based on non-background corrected raw counts
818 (background counts were negligible). The Al and Si maps reveal that the orthoclase-SAL chemical
819 interface is extremely sharp at the nm-scale, due to step function-like drops in their respective
820 concentrations in the SAL. The interface on the K map is less obvious, mainly because the concentration
821 gradient across the boundary is much less important, in particular at the interface in the upper part of
822 Fig. 9c. Calcium is distributed exclusively, but inhomogeneously, in the SAL. Calcium concentrations
823 are highest further away from the orthoclase interface, with lower levels present in the 70-nm thick part
824 of the SAL abutting the orthoclase. Note that the presence of tiny red-colored flecks on the orthoclase
825 surface is an artifact due to redeposition, and is not representative of any penetration of Ca into the
826 orthoclase structure (see previous discussion above).

827 The superposition of several elemental maps shown in Fig. 9b affords a multi-element view of the
828 sharp orthoclase-SAL interface, as well as how Ca, K, and Si are spatially co-distributed in the SAL. As
829 was the case in Fig. 9c, the chemical interface is spatially coincident with the mass-density interface in
830 Fig. 9a. The vertically oriented chemical interface between the unaltered orthoclase grain (blue, right
831 side) and the secondary precipitate (green and red, left side) is indicated by the white arrows. The
832 orthoclase does not have a homogeneous blue color, as indicated by the presence of green patches in the
833 lower half of the image- the possible reasons for this are discussed directly above. The transition from
834 orthoclase to SAL (i.e., blue to green) is in particular characterized by a sharp decrease in Si and
835 concomitant moderate increase in K. The SAL adjacent and to the left of the orthoclase interface is
836 characterized in particular by high levels of K (vivid green color), while further away ($> \sim 70$ nm) it is
837 enriched in Ca. Nonetheless, the distribution of red flecks within green, K-rich region indicates that Ca
838 is distributed throughout the SAL, even where it abuts the orthoclase interface. The decrease in K
839 concentrations roughly 70 nm distant from the interface corresponds to the predominance of the vivid
840 red color at the far left of the image, indicating higher Ca concentrations. The limit between K-rich and
841 Ca-rich regions in the SAL is irregular and not abrupt. Given the elevated Ca concentrations it is
842 possible that amorphous or nanocrystalline calcium carbonate is a component of SAL. In general, the
843 SAL also contains Si (and Al- see Fig. 9c), but at lower levels compared to the orthoclase (Si appears as
844 dark blue-purple within the SAL). We also remark that it is likely that the SAL is water-enriched, but
845 that quantification of H is not possible by EDXS.

846 The most significant finding here is the presence of this ~ 70 -nm wide K-enriched SAL that directly
847 contacts the orthoclase interface (note that the full thickness of the SAL is > 70 nm). To better compare
848 the overall chemistry of these adjacent phases, quantitative EDXS measurements of K, Al, Si and O

849 concentrations (X-ray absorption-corrected) were first made within the orthoclase (i.e. in the blue-
850 colored area to the right of the interface, Fig. 9b)- these yielded the nominal composition of unaltered
851 orthoclase, thereby indicating that the orthoclase retained its composition during alteration. Calcium
852 levels were below the analytical limit, evidence that Ca substitution or replacement of the orthoclase
853 structure did not occur. The same type of quantitative, X-ray absorption-corrected EDXS measurement
854 of the chemical composition of the SAL was effected in the rectangular area in Fig. 8b. The results are
855 given below and in Table 3 in atom % (atom % is preferred over weight % since atomic ratios can be
856 immediately compared to values derived from Table 1):

857 C = 6.5
858 Na = 0.74
859 Ca = 5.13
860 K = 11.41
861 Si = 15.94
862 Al = 4.81
863 O = 55.45

864
865 The chemical composition of the analyzed area confirms that the amorphous phase is very rich in K,
866 with a concentration significantly greater than that in the proximal unaltered orthoclase (i.e. XRF-
867 derived [$K_{\text{orthoclase CSY-1}}$] is 5.2 atom % - see Table 1). We note that the concentrations of Al and Si in the
868 SAL are 3 and 7 atom % less, respectively, than their XRF-measured concentrations in orthoclase
869 sample CSY-1 (Table 1). The average spectrum (not shown) corresponding to the rectangular area
870 reveals that the C K peak is convoluted with the K and Ca L peak; thus, the error in the quantitative
871 estimate for C (~10 %) is higher than for the other elements: Si, Al, K, Na, Ca, and O (~6 %).

872

873 3.3.6 Atomic resolution imaging of orthoclase-SAL interface

874 Numerous high-resolution TEM (HRTEM) images of the interfacial region (CSY-1C and CSY-3C)
875 always show a near-atomically sharp and relatively linear structural interface. Figure 10 is a typical
876 example of such an interface (white arrows)- the high-resolution image stems from an interface close to
877 that in Fig. 9. In this particular area, the amorphous layer is many tens of nm thick. Here one can see
878 lattice fringes terminating abruptly at the amorphous secondary precipitate. However, in some regions of
879 the interface, the fringes are blurry and appear to extend beyond the interface into the amorphous phase.
880 There are two possible reasons for this: a delocalization effect, or more probably, a highly inclined
881 (oblique) and/or non-planar, irregular interface. It should be remembered that the interface has a
882 considerable thickness, at least on the order of ~150 nm, which is the approximate thickness of the FIB

883 lamella. It is to be expected that over such a distance the interface will not be perfectly planar and
884 vertical. The non-crystallinity of the amorphous layer was verified by fast Fourier transform (FFT).

885

886 **4. Discussion of dissolution mechanism**

887 Our results show the ubiquitous presence of a continuous layer of amorphous material abutting
888 primary orthoclase grains. This SAL is variable in thickness, ranging from under ten nm to
889 approximately 200 nm. When imaged at moderate to high resolution, the structural interface between the
890 orthoclase and the SAL is sharp at the 1-2 nm scale, and is spatially coincident with a very abrupt
891 chemical boundary characterized by distinct decreases in Al and Si. The interface is also characterized
892 by important concentrations of Ca on the SAL side, and its virtual absence on the orthoclase side. Very
893 importantly, the SAL also contains variable and elevated concentrations of K. Our nm-scale
894 measurements point to a first-time observed K-rich authigenic phase that forms directly and in situ at the
895 receding interface of orthoclase during dissolution at alkaline conditions. This amorphous SAL is by far
896 a more significant reservoir of K than hitherto measured in previous studies.

897 In section 3.1 we report that one sample has a moderate amorphous content of ~16 mass % (sample
898 CSY-1C-a). Based on this measurement, we speculate that discreet amorphous phases also formed
899 elsewhere in the hydrothermal product, in particular within the amalgam of secondary authigenic phases.
900 We did not characterize these potential occurrences of amorphous material, as our investigation was
901 restricted to the interfacial region of orthoclase grains. As far as we know, the only comparable analysis
902 of an amorphous phase produced during alkaline alteration of a K-feldspar can be found in Ciceri et al.
903 (2017a). Their study revealed the presence of amorphous grains that contain on average 3.6 wt % K.

904 During chemical alteration the original orthoclase grains dissolve and decrease in volume and mass,
905 but at the nanometer to micron scale, the remaining orthoclase grain cores do not show evidence for
906 chemical alteration, as they retain their nominal, bulk chemical composition (section 3.3.5), even at
907 grain edges (Figs. 8, 9). In addition, all grain edges are characterized by sharp structural reaction
908 interfaces, as evidenced by orthoclase lattice fringes terminating abruptly at the boundary with the
909 SAL (Fig. 10). These two observations are evidence that dissolution is congruent (i.e. stoichiometric)
910 and proceeds via a sharp reaction front that consumes the parent orthoclase structure.

911 One immediate question that comes to mind is why K^+ , a labile cation, was not preferentially
912 leached from the orthoclase structure during alteration, thereby leading to the formation of K-deficient
913 leached layers? This traditional idea of leached layer formation during dissolution can be dismissed for
914 many reasons. First, the replacement of K^+ by H^+ (or H_3O^+) from the solution can be discounted because

915 the concentration of H^+ in the solvent is vanishingly small in a strong alkaline solution with very high
916 pH. This would render such an exchange process improbable. Moreover, leached layer formation is
917 controlled by interdiffusion (e.g., Hellmann et al., 2012; and references therein), and such a solid-state
918 process is orders of magnitude too slow at the 190 °C temperature of the experiments. And finally,
919 replacement of K^+ by H^+ would be incompatible with the orthoclase structure. Note that there is no
920 evidence of a change in lattice fringe spacing at the orthoclase edge in Fig., 10.

921 A second question we can ask is why K-Ca exchange did not occur, such as postulated by Ciceri et
922 al. (2017a). This would entail the preferential loss of K^+ from the orthoclase structure, coupled to an
923 interdiffusion-controlled substitution by Ca^{2+} ions from the solvent, leading to the in situ formation of a
924 Ca-rich plagioclase phase. A diffusion-controlled mineral replacement process would require evidence
925 for anti-correlated and sigmoidal interdiffusion-coupled Ca-K profiles (see, e.g. Hellmann et al., 2012).
926 Chemical analyses and nm-scale chemical mapping of the orthoclase interfacial region (Figs. 6, 9),
927 however, show no evidence for the penetration of Ca into the orthoclase structure. In addition to this, an
928 exchange process is theoretically difficult to envision due to the substantial size difference between
929 univalent K^+ and divalent Ca^{2+} . Moreover, the formation of Ca-plagioclase reaction rind ($KAlSi_3O_8 \rightarrow$
930 $CaAl_2Si_2O_8$) would also require a net addition of Al and a loss of Si to the original orthoclase structure.
931 Again, we see no evidence for a gain of Al and loss of Si in the orthoclase structure, in particular at grain
932 edges (Figs. 8, 9). As briefly mentioned above, a solid-state diffusive process at 190°C is simply too
933 slow to render such a change in chemistry over the 24 h time span of these experiments. It should be
934 remembered that solid-state diffusional processes are exceedingly slow compared to chemical reactions
935 such as dissolution and/or precipitation below ~500 °C (see, e.g., Villa, 2016). In fact, in nature the
936 solubility of Ca in K-feldspar at low temperatures is insignificant- only at higher temperatures can minor
937 amounts of Ca be incorporated into K-feldspar structures. This explains why, in fact, the unaltered K-
938 feldspars used in this study contain only trace amounts of Ca (Table 1).

939 The results we present strongly support a different mechanism that controls the hydrothermal
940 alkaline alteration of K-feldspar, and stands in opposition to nearly all previous studies in this field. As
941 elucidated in the Introduction (section 1.3), the prevailing opinion is that alteration of alkali feldspars
942 occurs either by congruent dissolution, or by preferential leaching of K and replacement by another
943 charge-compensating cation from solution. Our experimental results concur with the process of
944 congruent dissolution, which in turn is accompanied by precipitation of predominantly crystalline
945 secondary phases (calcite, hydrogrossular, tobermorite) from an oversaturated bulk solution. Where our
946 interpretation differs from nearly all other studies (at alkaline pH conditions) is that we have measured

947 the in situ formation of a significant amorphous phase that forms directly at the interface and at the
948 expense of the dissolving orthoclase structure. We postulate that this amorphous SAL starts to form right
949 at the onset of contact with the solvent fluid, and continues to form as the feldspar interface continuously
950 recedes during dissolution. The interfacial process we are proposing represents a physically plausible
951 process that concurs with our nm-scale observations and measurements. We refer to this process as
952 coupled interfacial dissolution-precipitation, or CIDR (Hellmann et al., 2003, 2012, 2015). As
953 discussed further on, this is a relatively new theory, and has been the subject of other chemical alteration
954 studies concerning both silicate minerals and glasses. This same mechanism has also been applied to
955 pseudomorphic mineral-mineral replacement reactions, where it has been referred to as interfacial-
956 coupled dissolution-(re)precipitation, or ICDP (Putnis, 2002; Putnis et al., 2005; Geisler et al., 2005; and
957 references therein).

958 Based on our finding of an abrupt and spatially coincident chemical and structural discontinuity
959 at the interface between the edge of the orthoclase structure and the amorphous SAL, we advocate the
960 CIDR mechanism (O'Neil and Taylor, 1967; Buck et al., 2000; Hellmann et al., 2003, 2012, 2015;
961 Putnis, 2002, 2009). This mechanism is based on the advance of a sharp chemical reaction front into the
962 unaltered parent phase, with stoichiometric dissolution occurring within a thin fluid film (O'Neil and
963 Taylor, 1967) of ordered solvent molecules (Thomä et al., 2019; Parker et al., 2001; Khatib et al., 2016)
964 at the reactive interface (Hellmann et al., 2015). Released elements that are insoluble synchronously
965 reprecipitate at the interface, without first passing into the bulk solution, whereas soluble elements
966 migrate to the bulk solution. The thin fluid film possesses physico-chemical and rheological properties
967 that differ from the bulk fluid (Fenter and Sturchio, 2004; Marry et al., 2008; Knight et al., 2019), and
968 thus reprecipitation of a secondary phase is possible even when the bulk solution is chemically under-
969 saturated with respect to secondary phases (Hellmann et al., 2003, 2012, 2015; Ruiz-Agudo et al., 2012).
970 The tight spatial and temporal coupling of dissolution and reprecipitation within an interfacial fluid film
971 is one of the main characteristics that differentiates CIDR from a classical precipitation process
972 associated with a chemically oversaturated bulk solution.

973 How and when the amorphous phase formed is a key to understanding the overall dissolution
974 process in our study, and in particular, the mechanism of dissolution. The spatial ordering of the
975 secondary phases shows that the amorphous phase was initially the first phase to form. With increasing
976 reaction progress, secondary crystalline phases started to massively precipitate on top of the amorphous
977 SAL as the bulk fluid became increasingly saturated with solute. The reasons for chemical
978 oversaturation are multiple: dissolution of the orthoclase grains, a steadily decreasing fluid-solid ratio,
979 cooling at the end of the experiment, and finally, evaporation of any remaining fluid during the final heat

980 treatment step. All of these contributed to chemical supersaturation of the bulk solution and the classical
981 precipitation of the secondary crystalline phases. It is interesting to note that the overall morphology of
982 our reacted orthoclase grains, characterized by a relatively thin amorphous SAL overlain by a 1-2 μm
983 thick rind of secondary crystalline phases, has a counterpart in a study of a naturally altered K-feldspar
984 that has a 10 nm-thick amorphous SAL covered by a thick 3-5 μm layer of authigenic smectite (Zhu et
985 al., 2006).

986 The experimental protocol did not permit us to periodically sample the solution phase, nor
987 retrieve orthoclase grains before the end of each experiment. Nonetheless, we argue that the amorphous
988 phase is not a classical precipitate, but rather formed in situ by CIDR, and its growth was initiated upon
989 contact of the fluid with the orthoclase grains. Based on solubility arguments, if the amorphous phase
990 had been a classical precipitate, it would have formed on top of the less soluble secondary crystalline
991 phases, but the FESEM and TEM images clearly show that this was not the case. In addition, we use
992 experimental data from a previous study (Hellmann, 1995) to further this argument. In that particular
993 study, the release of Na, Al and Si was continuously measured during hydrothermal alteration of albite
994 feldspar in a flow reactor at 200 °C and pH 12 KOH solution- we note that albite and orthoclase have
995 similar structures; in addition, the alteration conditions were very close to those in the present study.
996 While a mechanism describing how the parent solid reacts cannot be deduced solely from aqueous
997 cation release curves, the release curves do show that right from the beginning of the experiment, the
998 aqueous solutions show non-stoichiometry (Hellmann, 1999b), even though the solution was very
999 undersaturated with respect to secondary crystalline phases. This data by itself can be interpreted to
1000 mean that a surface interfacial process was continuously operative in the experiment by Hellmann
1001 (1995). Going further, the Hellmann data supports our argument that an interfacial process starting right
1002 at the onset, and continuing throughout the experiment, resulted in interfacial precipitation of an
1003 amorphous SAL. Other studies in the literature concur with this idea, namely those that have measured
1004 dissolution in situ. These published experiments, at ambient and hydrothermal conditions, have
1005 measured in real time and in situ the initial reaction between silicate minerals and aqueous fluids
1006 (Hellmann, 1999a; Hellmann et al., 1992; Putnis et al., 2005; Ruiz-Agudo et al., 2012; Jordan et al.,
1007 1999; Fenter et al., 2000; Teng et al., 2001; Leonard and Hellmann, 2017). These studies all show the
1008 rapid in situ formation of a surficial gel-like phase that is an amorphous interfacial reprecipitate.

1009 It is interesting to speculate why we did not document a pseudomorphic replacement reaction
1010 involving a Ca-rich plagioclase. Feldspar-feldspar replacement reactions in nature and experiment are
1011 widely cited (O'Neil and Taylor, 1967; Parsons and Lee, 2009; Parsons et al., 2009; Lee and Parsons,
1012 1997; Labotka et al., 2004; Cole et al., 2004; Engvik et al., 2008; Hövelmann et al., 2010; Norberg et al.,

2013 2011; Ruiz-Agudo et al., 2014). Because CIDR is a fluid-assisted alteration process that is thought to
2014 occur in a thin interfacial fluid film, it is theoretically possible that a Ca-rich crystalline phase, such as
2015 Ca-rich plagioclase (labradorite, anorthite), could have formed at the reactive interface- as the argument
2016 of Ca^{+2} and K^{+} incompatibility due to ionic radius and charge, as well as too slow solid-state
2017 interdiffusion, would not be relevant. However, in our study, the SAL that formed was amorphous.
2018 Given that CIDR is a fluid-mediated chemical alteration mechanism, and not a solid-state process, it
2019 should be possible from a strictly theoretical point of view to form a Ca-rich plagioclase phase within
2020 the interfacial fluid, provided that the chemical components are present in the correct stoichiometric
2021 proportions and concentrations. However, there was no evidence for this having occurred. At this point
2022 we can only surmise a few reasons that possibly favored reprecipitation of an amorphous phase: *i.* a too
2023 low Ca concentration, *ii.* an extremely basic pH (12.4 $T=25$ °C), *iii.* a too low temperature (190 °C) coupled
2024 to a very short time period (24 h). Perhaps over geological periods of time and at much higher
2025 temperatures, it may be possible to precipitate a Ca-rich plagioclase phase in the context of a mineral-
2026 mineral replacement reaction. Future experiments at higher T , P conditions, or over longer time periods,
2027 could perhaps answer this question. It is interesting to note that the reverse process, the albitization of
2028 plagioclase, has been experimentally documented at 600 °C, 2 kbars in an aqueous Na-silicate solution
2029 (Hövelmann et al., 2010).

2030 Many frontier questions on the CIDR mechanism still remain. Since the reprecipitated layer
2031 initially forms at the interface, presumably within the extremely thin interfacial fluid film in contact with
2032 the parent mineral structure, it remains to be determined whether this fluid film of ordered solvent
2033 molecules is continuous, or not. During chemical alteration, the dissolution of the primary phase
2034 (orthoclase) is a continuous process, and it is at the ‘inner edge’ of the SAL where new material is
2035 precipitated. The chemical stability of the reprecipitated material within the thin fluid film will in large
2036 part determine its chemical composition. Although we don’t know what the pH was in the fluid film, it
2037 was undoubtedly very basic (close to the value in the bulk fluid), and at such conditions, Si and Al
2038 oxides or oxyhydroxides are very soluble. This may explain the lower levels of Al and Si that were
2039 measured in the SAL, as compared to their nominal concentrations in orthoclase. Nonetheless, the Si and
2040 Al that did precipitate in the layer (i.e., Fig. 9) would likely be in the form of Si-O^{-} and Al-O^{-} groups, as
2041 these groups predominate at very basic pH conditions. Released K^{+} ions may preferentially adsorb to
2042 these negatively charged sites. It nonetheless remains an open question as to why the K concentration in
2043 the SAL is so conspicuously elevated. As the amorphous layer grows in thickness over time, the first-
2044 formed and older ‘outer edge’ will be in contact with the free bulk fluid, or fluid within pores and
2045 channels of any overlying secondary crystalline precipitates that formed. Therefore, the chemical

1046 stability of the outer interface of the SAL, which controls its dissolution behavior, will be dictated by the
1047 chemical properties of the bulk fluid, and not the thin interfacial fluid film. A more detailed
1048 understanding of the composition and exact nature of the amorphous interfacial layer calls for additional
1049 research, in particular using other complementary techniques, such as X-ray adsorption or
1050 nanoRaman/FTIR. One last question that perhaps deserves further study is whether the amorphous SAL,
1051 as well as the enveloping rind of secondary authigenic minerals, eventually hinder, or at least slow
1052 down, the kinetics of the orthoclase dissolution reaction. A similar question was also posed by Zhu et al.
1053 (2006) concerning their estimation that a naturally weathering Jurassic-aged K-feldspar was dissolving 5
1054 orders of magnitude slower than K-feldspar in far-from-equilibrium laboratory experiments at
1055 comparable pH and *T* conditions. They attributed this significant difference to the presence of a 10 nm-
1056 thick amorphous SAL, surface-adhering kaolin platelets, and a thick outer rind of authigenic smectite.

1057

1058 **5. Conclusions**

1059 To extend our thoughts concerning the present study, an interfacial amorphous phase has been
1060 documented to form in situ at the expense of orthoclase at strong alkaline conditions. Amorphous SALs
1061 have been previously documented to form on feldspars at acid, near-neutral and weak alkaline pH
1062 conditions, with pH controlling their thickness. They are significantly thicker at acid pH than those that
1063 form at near-neutral and moderate basic pH (Hellmann et al., 2003, 2012; Lee et al., 2007). As discussed
1064 in detail in section 1.3, the majority of studies on feldspars from the 1990s and early 2000s postulated
1065 that SALs (even when very thin) form by an interdiffusion process, leading to leached layers. Despite
1066 the pioneering study of O'Neil and Taylor in 1967, it has only been over the past 20 years that natural
1067 and experimental feldspar dissolution studies at acid and near-neutral pH conditions, and in particular
1068 amorphous SAL and mineral-mineral replacement reactions, have been conceptually framed within the
1069 context of CIDR and CIDR-like mechanisms (e.g., Hellmann et al., 2003, 2012; Lee et al., 2007;
1070 Parsons and Lee, 2009; Labotka et al., 2004; Hövelmann et al., 2010; Ruiz-Agudo et al., 2014). A
1071 theoretical Monte Carlo approach also supports the CIDR mechanism for plagioclase dissolution
1072 mechanisms (Zhang and Lüttge, 2009). Perhaps the most significant contribution our new data make is
1073 filling an important knowledge gap on the mechanism of K-feldspar dissolution in strong alkaline
1074 solutions. Thus, this study can be considered to be a unifying element in terms of the dissolution process
1075 of alkali feldspars over the full range of pH conditions, and at temperatures up to an including
1076 hydrothermal conditions. Only further research will contribute to answering the question as to whether
1077 CIDR is a generic and universal mechanism of chemical alteration for all feldspars and other silicate

1078 minerals in aqueous solutions over a broad range of pH and temperature conditions.

1079

1080

1081

1082

1083

1084 **Acknowledgements**

1085 The initial phase of this study was supported by Projects in the National Science & Technology Pillar
1086 Program during the Eleventh Five-Year Plan Period (China, No. 2006BAD10B04) and the Knowledge
1087 Innovation Project of the Chinese Academy of Sciences and the Spark Program of China (No.
1088 2007EA173003). The aforementioned funding covered the procurement of the orthoclase samples in the
1089 field, chemical characterization by X-ray fluorescence, hydrothermal alteration in the laboratory, and
1090 leaching experiments followed by aqueous ICP analyses. The one-year stay of YZ (Nov. 2017-Nov.
1091 2018) with the RH research group at ISTERre, Grenoble, France was financed by a State Scholarship
1092 Fund organized by the China Scholarship Council. The analytical, instrumental, and travel costs in
1093 France were supported by two ISTERre-BQR grants. B. Lanson's (ISTERre) expertise with XRD and
1094 Rietveld refinement is gratefully acknowledged, as is the valuable assistance for the BET analyses by V.
1095 Magnin (ISTERre). The geochemistry-mineralogy platform of ISTERre is partially funded by a grant from
1096 Labex OSUG@2020 (investissements d'avenir, ANR10-LABX56). We are particularly thankful for the
1097 FIB, FESEM and TEM beam time provided by Section 3.5, Interface Geochemistry (head: L. Benning),
1098 GFZ Potsdam, Germany. The financial support of the Helmholtz Recruiting Initiative (grant No. I-044-
1099 16-01) is acknowledged. We also thank J. Hughes (Univ. Vermont) for useful discussions. We thank an
1100 anonymous reviewer and the chief editor, M. Böttcher, for helpful comments that improved the
1101 manuscript.

1102

1103 **References**

- 1104 Arnold, G.W., Westrich, H.R., Casey, W.H., 1992. Application of ion beam analysis (RBS and ERD) to the surface chemistry
1105 study of leached minerals. *Nuclear Instruments Methods Phys. Res.*, B 64, 542–546.
- 1106
- 1107 Bandstra, J.Z., Buss, H.L., Campen, R.K., Liermann, L.J., Moore, J., Hausrath, E.M., Navarre-Sitchler, A.K., Jang, J. H.,
1108 Brantley, S.L., 2008. Appendix: Compilation of mineral dissolution rates. In: Brantley, S.L., Kubicki, J.D., White, A.F.
1109 (Eds.), *Kinetics of Water-Rock Interaction*, Springer, New York, pp. 737–823.
- 1110
- 1111 Bergmann, J. (2005) Rietveld Analysis Program BGMN (http://www.bgm.de/BGMN_manual_2005.pdf).
- 1112
- 1113 Blum, A.E., Stillings, L.L., 1995. Feldspar dissolution kinetics. In: White, A.F., Brantley, S.L. (Eds.), *Chemical Weathering
1114 Rates of Silicate Minerals*. Mineralogical Society of America, Washington, D.C., pp. 291–351.
- 1115
- 1116 Brown, W.L., Parsons, I., 1989, Alkali feldspars: ordering rates, phase transformations and behavior diagrams for igneous
1117 rocks. *Mineral. Mag.* 53, 25-42.
- 1118
- 1119 Buck, E.C., Smith, K.L., Blackford, M.G., 2000. The behavior of silicon and boron in the surface of corroded nuclear
1120 waste glasses: An Eftem Study. *Mat. Res. Soc. Symp. Proc.* 608, 727-732.
- 1121
- 1122 Casey, W.H., Westrich, H.R., Arnold, G.W., 1988. Surface chemistry of labradorite feldspar reacted with aqueous solutions at
1123 pH = 2, 3, and 12. *Geochim. Cosmochim. Acta* 52, 2795-2807.
- 1124

- 1125 Casey, W.H., Westrich, H.R., Arnold, G.W., Banfield, J.F., 1989a. The surface chemistry of dissolving labradorite feldspar.
1126 *Geochim. Cosmochim. Acta* 53, 821-832.
- 1127
1128 Casey, W.H., Westrich, H.R., Massis, T., Banfield, J.F., Arnold, G.W., 1989b. The surface of labradorite feldspar after acid
1129 hydrolysis. *Chem. Geol.* 78, 205-218.
- 1130
1131 Chen, Y., Brantley, S.L., Ilton, E.S., 2000. X-ray photoelectron spectroscopic measurement of the temperature dependence of
1132 leaching of cations from the albite surface. *Chem. Geol.* 163, 115-128.
- 1133
1134 Ciceri, D., de Oliveira, M., Allanore, A., 2017a. Potassium fertilizer via hydrothermal alteration of K-feldspar ore. *Green*
1135 *Chem.* 19, 5187–5202.
- 1136
1137 Ciceri, D., Manning, D.A.C., Allanore, A., 2015. Historical and technical developments of potassium resources. *Sci. Total*
1138 *Environm.* 502, 590–601.
- 1139
1140 Ciceri, D., Oliveira, M.d., Stokes, R.M., Skorina, T., Allanore, A., 2017b. Characterization of potassium agrominerals:
1141 Correlations between petrographic features, comminution and leaching of ultrapotassic syenites. *Mins. Eng.* 102, 42-57.
- 1142
1143 Cliff, G., Lorimer, G.W., 1975. The quantitative analysis of thin specimens. *J. Micros.* 103, 203–207.
- 1144
1145 Chou, L., Wollast, R., 1985. Steady-state kinetics and dissolution mechanisms of albite. *Am. J. Sci.* 285, 963-993.
- 1146
1147 Cole, D.R., Larson, P.B., Riciputi, L.R., Mora, C.I., 2004. Oxygen isotopes zoning profiles in hydrothermally altered
1148 feldspars: estimating the duration of water-rock interaction. *Geology* 32, 29–32.
- 1149
1150 de la Torre, A.G., Bruque, S., Aranda, M.A.G., 2001. Rietveld quantitative amorphous content analysis. *J. Appl. Cryst.* 34,
1151 196–202.
- 1152
1153 Döbelin, N., Kleeberg, R., 2015. Profex: a graphical user interface for the Rietveld refinement program BGMN. *J. Appl.*
1154 *Cryst.* 48, 1573–1580.
- 1155
1156 Dran, J.-C., Della Mea, G., Paccagnella, A., Petit, J.-C., Trotignon, L., 1988. The aqueous dissolution of alkali silicate glasses:
1157 reappraisal of mechanisms by H and Na depth profiling with high energy ion beams. *Phys. Chem. Glasses* 29, 249-255.
- 1158
1159 Engvik, A.K., Putnis, A., Gerald, J.D.F., Austrheim, H., 2008. Albitization of granitic rocks: the mechanism of replacement
1160 of oligoclase by albite. *Can. Miner.* 46, 1401–1415.
- 1161
1162 Fenter, P., Sturchio, N.C., 2004. Mineral-water interfacial structures revealed by synchrotron X-ray scattering.
1163 *Progress Surf. Sci.* 77, 171-258.
- 1164
1165 Fenter, P., Lee, S.S., Park, C., Catalano, J.G., Zhang, Z., Sturchio, N.C., 2010. Probing interfacial reactions with X-ray
1166 reflectivity and X-ray reflection interface microscopy: Influence of NaCl on the dissolution of orthoclase at pOH 2 and 85 °C.
1167 *Geochim. Cosmochim. Acta* 74, 3396–3411.
- 1168
1169 Fenter, P., Teng, H., Geissbühler, P., Hanchar, J.M., Sturchio, N.C., 2000. Atomic-scale structure of the orthoclase (001)-
1170 water interface measured with high-resolution X-ray reflectivity. *Geochim. Cosmochim. Acta* 64, 3663–3673.
- 1171
1172 Gautier, J.-M., Oelkers, E.H., Schott, J., 1994. Experimental study of K-feldspar dissolution rates as a function of chemical
1173 affinity at 150°C and pH 9. *Geochim. Cosmochim. Acta* 58, 4549-4560.
- 1174
1175 Geisler, T., Pöml, P., Stephan, T., Janssen, A., Putnis, A., 2005. Experimental observation of an interface-controlled
1176 pseudomorphic replacement reaction in a natural crystalline pyrochlore. *Amer. Mineral.* 90, 1683-1687.
- 1177
1178 Grogger, W., Schaffer, B., Krishnan, K.M., Hofer, F., 2003. Energy-filtering TEM at high magnification: spatial resolution
1179 and detection limits. *Ultramicroscopy*, 96, 481–489.
- 1180
1181 Harlov, D.E., Förster, H.-J., Nijland, T.G., 2002. Fluid-induced nucleation of (Y + REE)-phosphate minerals within apatite:
1182 Nature and experiment. Part I. Chlorapatite. *Amer. Miner.* 87, 245–261.
- 1183

- 1184 Hellmann, R., 1994. The albite-water system: Part I. The kinetics of dissolution as a function of pH at 100, 200, and 300°C.
 1185 *Geochim. Cosmochim. Acta* 58, 595–611.
 1186
- 1187 Hellmann, R., 1995. The albite-water system: Part II. The time-evolution of the stoichiometry of dissolution as a function of
 1188 pH at 100, 200 and 300°C. *Geochim. Cosmochim. Acta* 59, 1669–1697.
 1189
- 1190 Hellmann, R., 1999a. The dissolution behavior of albite feldspar at elevated temperatures and pressures: the role of surface
 1191 charge and speciation. *Mitt. Österr. Mineral. Ges.* 144, 13–44.
 1192
- 1193 Hellmann, R., 1999b. Stoichiometry. In: Marshall, C.P., Fairbridge, R.W. (Eds.), *Encyclopedia of Geochemistry*, Kluwer
 1194 Academic Publishers, pp. 595–598.
 1195
- 1196 Hellmann, R., Crerar, D.A., Zhang, R.H., 1989. Albite feldspar hydrolysis to 300 °C. *Solid State Ionics* 32/33, 314–329.
 1197
- 1198 Hellmann, R., Drake, B., Kjoller, K., 1992. Using atomic force microscopy to study the structure, topography and dissolution
 1199 of albite surfaces. In: Kharaka, Y.K., Maest, A.S. (Eds.), *Water-Rock Interaction 7 Vol. I.*, Balkema, Rotterdam, pp. 149–
 1200 152.
 1201
- 1202 Hellmann, R., Dran, J.-C., Della Mea, G., 1997. The albite-water system Part III. Characterization of leached and
 1203 hydrogen-enriched layers formed at 300°C using MeV ion beam techniques. *Geochim. Cosmochim. Acta* 61, 1575–1594.
 1204
- 1205 Hellmann, R., Eggleston, C.M., Hochella, M. F., Jr., Crerar, D. A., 1990. The formation of leached layers on albite surfaces
 1206 during dissolution under hydrothermal conditions. *Geochim. Cosmochim. Acta* 54, 1267–1281.
 1207
- 1208 Hellmann, R., Penisson, J.-M., Hervig, R.L., Thomassin, J.-H., Abrioux, M.-F., 2003. An EFTEM/HRTEM high-resolution
 1209 study of the near surface of labradorite feldspar altered at acid pH: evidence for interfacial dissolution-precipitation. *Phys.*
 1210 *Chem. Mins.* 30, 192–197.
 1211
- 1212 Hellmann, R., Wirth, R., Daval, D., Barnes, J.-P., Penisson, J.-M., Tisserand, D., Epicier, T., Florin, B., Hervig, R.L., 2012.
 1213 Unifying natural and laboratory chemical weathering with interfacial dissolution–precipitation: A study based on the
 1214 nanometer-scale chemistry of fluid–silicate interfaces. *Chem. Geol.* 294–295, 203–216.
 1215
- 1216 Hellmann, R., Cotte, S., Cadel, E., Malladi, S., Karlsson, L.S., Lozano-Perez, S., Cabié, M., Seyeux, A., 2015. Nanometre-
 1217 scale evidence for interfacial dissolution–precipitation control of silicate glass corrosion. *Nature Materials* 14, 307–311.
 1218
- 1219 Holdren, G.R., Jr., Speyer, P.M., 1985. pH dependent changes in the rates and stoichiometry of dissolution of an alkali
 1220 feldspar at room temperature. *Am. J. Sci.* 285, 994–1026.
 1221
- 1222 Hövelmann, J., Putnis, A., Geisler, T., Schmidt, B.C., Golla-Schinder, U., 2010. The replacement of plagioclase feldspars by
 1223 albite: observations from hydrothermal experiments. *Contrib. Miner. Petrol.* 159, 43–59.
 1224
- 1225 Jordan, G., Higgins, S.R., Eggleston C.M., Swapp, S.M., Janney, D.E., Knauss, K.G., 1999. Acidic dissolution of
 1226 plagioclase: In-situ observations by hydrothermal atomic force microscopy. *Geochim. Cosmochim. Acta* 63, 3183–3191.
 1227
- 1228 Kasiopas, A., Perdikouri, C., Putnis, C.V., Putnis, A., 2008. Pseudomorphic replacement of single calcium carbonate crystals
 1229 by polycrystalline apatite. *Mineral. Mag.* 72, 77–80.
 1230
- 1231 Khatib, R., Backus, E.H., Bonn, M., Perez-Haro, M.J., Gaigeot, M.P., Sulpizi, M., 2016. Water orientation and hydrogen-
 1232 bond structure at the fluorite/water interface. *Sci. Reports* 6, 24287.
 1233
- 1234 King, H.E., Plümper, O., Geisler, T., Putnis, A., 2011. Experimental investigations into the silicification of olivine: Implications for
 1235 the reaction mechanism and acid neutralization. *Amer. Mineral.* 96, 1503–1511.
 1236
- 1237 Klein, C., Philpotts, A.R., 2017. *Earth Materials: Introduction to Mineralogy and Petrology*. In: Klein, C., Philpotts, A.R.
 1238 (Eds.), Cambridge University Press, New York.
 1239
- 1240 Knight, A.W., Kalugin, N.G., Coker, E., Ilgen, A.G., 2019. Water properties under nano-scale confinement. *Sci. Reports* 9,
 1241 8246.
 1242

- 1243 Labotka, T.C., Cole, D.R., Fayek, M., Riciputi, L.R., Stadermann, F.J., 2004. Coupled cation and oxygen-isotope exchange
1244 between alkali feldspar and aqueous chloride solution. *Amer. Mineral.* 89, 1822–1825.
1245
- 1246 Lee, M.R., Parsons, I., 1997. Dislocation formation and albitization in alkali feldspars from the Shap granite. *Amer. Mineral.*
1247 82, 557–570.
1248
- 1249 Lee, M.R., Hodson, M.E., Parsons, I., 1998. The role of intragranular microtextures and microstructures in chemical and
1250 mechanical weathering: direct comparisons of experimentally and naturally weathered alkali feldspars. *Geochim. Cosmochim. Acta*
1251 62, 2771–2788.
1252
- 1253 Lee, M.R., Brown, D.J., Smith, C.L., Hodson, M.E., Mackenzie, M., Hellmann, R., 2007. Characterization of mineral
1254 surfaces using FIB and TEM: A case study of naturally weathered alkali feldspars. *Amer. Mineral.* 92, 1383–1394.
1255
- 1256 Lee, M.R., Hodson, M.E., Brown, D.J., MacKenzie, M., Smith, C.L., 2008. The composition and crystallinity of the
1257 near-surface regions of weathered alkali feldspars. *Geochim. Cosmochim. Acta* 72, 4962–4975.
1258
- 1259 Leonard, D.N., Hellmann, R., 2017. Exploring dynamic surface processes during silicate mineral (wollastonite) dissolution
1260 with liquid cell TEM. *J. Microsc.* 265, 358–371.
1261
- 1262 Liu, S. K., Han, C., Liu, J. M., Li, H. (2015) Hydrothermal decomposition of potassium feldspar under alkaline conditions.
1263 *RSC Advances* 5, 93301–93309.
1264
- 1265 Liu, S.K., Han, C., Liu, J.M., 2018. Study of K-feldspar and lime hydrothermal reaction at 190 °C: Phase, kinetics and
1266 mechanism with reaction time. *ChemistrySelect* 3, 13010–13016.
1267
- 1268 Liu, S.K., Han, C., Liu, J.M., 2019. Study of K-feldspar and lime hydrothermal reaction: Phase and mechanism with reaction
1269 temperature and increasing Ca/Si ratio. *Minerals* 9, 46.
1270
- 1271 Locati, F., Marfil, S., Baldo, E., Maiza, P., 2010. Na₂O, K₂O, SiO₂ and Al₂O₃ release from potassic and calcic–sodic feldspars
1272 into alkaline solutions. *Cement Concrete Res.* 40, 1189–1196.
1273
- 1274 Ma H.W., Yang J., Su S.Q., Liu M.T., Zheng H., Wang Y.B., Qi H.B., Zhang P., Yao W.G., 2015. 20 years advances in
1275 preparation of potassium salts from potassic rocks: A review. *Acta Geologica Sinica (Eng. Ed.)* 89, 2058–2071.
1276
- 1277 Marry, V., Rotenberg, B., Turq, P., 2008. Structure and dynamics of water at a clay surface from molecular dynamics
1278 simulation. *Phys. Chem. Chem. Phys.* 10, 4802–4813.
1279
- 1280 Martin, J.M., Vacher, B., Ponsonnet, L., Dupuis, V., 1996. Chemical bond mapping of carbon by image-spectrum EELS in
1281 the second derivative mode. *Ultramicroscopy* 65, 229–238.
1282
- 1283 Nesbitt, H.W., Muir, I.J., 1988. SIMS depth profiles of weathered plagioclase, and processes affecting dissolved Al and Si
1284 in some acidic soil conditions. *Nature* 334, 336–338.
1285
- 1286 Norberg, N., Neusser, G., Wirth, R., Harlov, D., 2011. Microstructural evolution during experimental albitization of K-rich
1287 alkali feldspar. *Contrib. Mineral. Petrol.* 162, 531–546.
1288
- 1289 Nugent, M.A., Brantley, S.L., Pantano, C.G., Maurice, P.A., 1998. The influence of natural mineral coatings on feldspar
1290 weathering. *Nature* 395, 588–591.
1291
- 1292 O'Neil, J.R., Taylor, H.P.J., 1967. The oxygen isotope and cation exchange chemistry of feldspars. *Amer. Mineral.* 52, 1414–
1293 1437.
1294
- 1295 Parker, S.C., de Leeuw, N.H., Bourova, E., Cooke, D.J., 2001. Molecular Modeling Theory: Applications in the
1296 Geosciences. In: Cygan, R.T., Kubicki, J.D. (Eds.), *Reviews in Mineralogy and Geochemistry*, Geochemical Society and
1297 Mineralogical Society of America, 42, pp. 63–82.
1298
- 1299 Parsons, I., Lee, M.R., 2009. Mutual replacement reactions in alkali feldspars I: microtextures and mechanisms. *Contrib.*
1300 *Mineral. Petrol.* 157, 641–661.
1301

- 1302 Parsons, I., Magee, C.W., Allen, C.M., Shelley, J.M.G., Lee, M.R., 2009. Mutual replacement reactions in alkali feldspars II:
1303 trace element partitioning and geothermometry. *Contrib. Mineral. Petrol.* 157, 663–687.
1304
- 1305 Petit, J.-C., Dran, J.-C., Schott, J., Della Mea, G., 1989. New evidence on the dissolution mechanism of crystalline silicates
1306 by MeV ion beam techniques. *Chem. Geol.* 76, 365-369.
1307
- 1308 Petit, J.-C., Dran, J.-C., Della Mea, G., 1990a. Energetic ion beam analysis in the Earth sciences. *Nature* 344, 621-626.
1309
- 1310 Petit, J.-C., Della Mea, G., Dran, J.-C., Magonthier, M.-C., Mando, P.A., Paccagnella, A., 1990b. Hydrated layer formation
1311 during dissolution of complex silicate glasses and minerals. *Geochim. Cosmochim. Acta* 54, 1941-1955.
1312
- 1313 Putnis, A., 2002. Mineral replacement reactions: from macroscopic observations to microscopic mechanisms. *Mineral. Mag.*
1314 66, 689–708.
1315
- 1316 Putnis, A., 2009. Mineral replacement reactions. In: Oelkers, E.H., Schott, J. (Eds.), *Reviews in Mineralogy and*
1317 *Geochemistry*, Mineralogical Society of America, 70, pp. 87–124.
1318
- 1319 Putnis, A., 2014. Why mineral interfaces matter. *Science* 343, 1441-1442.
1320
- 1321 Putnis, C.V., Mezger, K., 2004. A mechanism of mineral replacement: Isotope tracing in the model system KCl-KBr-H₂O.
1322 *Geochim. Cosmochim. Acta* 68, 2839–2848.
1323
- 1324 Putnis, C.V., Tsukamoto, K., Nishimura, Y., 2005. Direct observations of pseudomorphism: compositional and textural
1325 evolution at a fluid-solid interface. *Amer. Mineral.* 90, 1909–1912.
1326
- 1327 Robin, E., 2017. Method for the determination of the mass thickness and the composition of a zone of an object using an
1328 electron beam and measurements of X-ray intensities. France patent EP 3 032 244 B1.
1329
- 1330 Ruiz-Agudo, E., Putnis, C.V., Putnis, A., 2014. Coupled dissolution and precipitation at mineral–fluid interfaces. *Chem.*
1331 *Geol.* 383, 132–146.
1332
- 1333 Ruiz-Agudo, E., Putnis, C.V., Rodriguez-Navarro, C., Putnis, A., 2012. Mechanism of leached layer formation during
1334 chemical weathering of silicate minerals. *Geology* 40, 947–950.
1335
- 1336 Schweda, P., Sjöberg, L., Södervall, U., 1997. Near-surface composition of acid-leached labradorite investigated by SIMS.
1337 *Geochim. Cosmochim. Acta* 61, 1985-1994.
1338
- 1339 Skorina, T., Allanore, A., 2015. Aqueous alteration of potassium-bearing aluminosilicate minerals: from mechanism to
1340 processing. *Green Chem.* 17, 2123–2136.
1341
- 1342 Su, S.Q., Ma, H.W., Chuan, X.Y., 2015. Hydrothermal decomposition of K-feldspar in KOH–NaOH–H₂O medium.
1343 *Hydrometallurgy* 156, 47–52.
1344
- 1345 Teng, H.H., Fenter, P., Cheng, L., Sturchio, N.C., 2001. Resolving orthoclase dissolution processes with atomic force
1346 microscopy and X-ray reflectivity. *Geochim. Cosmochim. Acta* 65, 3459–3474.
1347
- 1348 Thomä, S.L.J., Krauss, S.W., Eckardt, M., Chater, P., Zobel, M., 2019. Atomic insight into hydration shells around faceted
1349 nanoparticles. *Nature Commun.* 10, 995.
1350
- 1351 Thomassin, J.-H., Le Coustumer, P., Patrier, P., 1995. Mineralogy and ultrastructure of some alteration products of
1352 Yamamoto-86032 meteorite. *Proc. NIPR Symp. Antarc. Meteorites* 8, 185-193.
1353
- 1354 van der Pluijm, B.A., Lee, J.H., Peacor, D.R., 1988. Analytical electron microscopy and the problem of potassium diffusion.
1355 *Clays Clay Minerals*, 36.
1356
- 1357 Villa, I.M., 2016. Diffusion in mineral geochronometers: Present and absent. *Chem. Geol.* 420, 1-10.
1358
- 1359 Watanabe, M., Williams, D.B., 2006. The quantitative analysis of thin specimens: a review of progress from the Cliff-
1360 Lorimer to the new ζ -factor methods. *J. Microsc.* 221, 89–109.

1361
1362 Williams, D. B., Carter, C.B., 2009. *Transmission Electron Microscopy Part 4: Spectrometry*, Springer.
1363
1364 Wirth, R., 2004. Focused Ion Beam (FIB): A novel technology for advanced application of micro- and nanoanalysis in
1365 geosciences and applied mineralogy. *Eur. J. Mineral.* 16, 863-876.
1366
1367 Wirth, R., 2009. Focused Ion Beam (FIB) combined with SEM and TEM: Advanced analytical tools for studies of chemical
1368 composition, microstructure and crystal structure in geomaterials on a nanometre scale. *Chem. Geol.* 261, 217–229.

1369
1370 Yang, Y., Min, Y., Jun, Y.S., 2013. A mechanistic understanding of plagioclase dissolution based on Al occupancy and T–O
bond length: from geologic carbon sequestration to ambient conditions. *Phys. Chem. Chem. Phys.* 15 (42), 18491–18501.

1371
1372 Yang, Y., Min, Y., Jun, Y., 2014a. Effects of Al/Si ordering on feldspar dissolution: part II. The pH dependence of
1373 plagioclases' dissolution rates. *Geochim. Cosmochim. Acta* 126, 595–613.

1374
1375 Yang, Y., Min, Y., Lococo, J., Jun, Y., 2014b. Effects of Al/Si ordering on feldspar dissolution: part I. Crystallographic
1376 control on the stoichiometry of dissolution reaction. *Geochim. Cosmochim. Acta* 126, 574–594.

1377
1378 Yuan, B., Li, C., Liang, B., Lü, L., Yue, H., Sheng, H., Ye, L., Xie, H., 2015. Extraction of potassium from K-feldspar
1379 via the CaCl₂ calcination route. *Chinese J. Chem. Eng.* 23, 1557-1564.

1380
1381 Zhai, Y., Hellmann, R., Campos, A., Findling, N., Mayanna, S., Wirth, R., Schreiber, A., Cabié, M., Zeng, Q., Liu, S., Liu, J., 2021.
1382 Fertilizer derived from alkaline hydrothermal alteration of K-feldspar: A micrometer to nanometer-scale investigation of K in
1383 secondary reaction products and the feldspar interface. *Applied Geochem.*

1384
1385 Zhang, L., Lüttge, A., 2009. Theoretical approach to evaluating plagioclase dissolution mechanisms. *Geochim. Cosmochim.*
1386 *Acta* 73, 2832-2849.

1387
1388 Zhu, C., Veblen, D.R., Blum, A.E., Chipera, S.J., 2006. Naturally weathered feldspar surfaces in the Navajo Sandstone
1389 aquifer, Black Mesa, Arizona: electron microscopic characterization. *Geochim. Cosmochim. Acta* 70, 4600-4616.

1390
1391
1392
1393
1394
1395
1396

1397
1398
1399

Table 1. Chemical compositions of unaltered orthoclase samples based on XRF analyses (mass %)

Sample ID	Locality*	SiO ₂	TiO ₂	Al ₂ O ₃	Fe ₂ O ₃ [†]	MnO	MgO	CaO	Na ₂ O	K ₂ O	P ₂ O ₅	LOI	Chemical formula
CSY-1 (#6)	Xinghe	65.96	0.02	18.39	0.22	0.01	0.05	0.22	2.96	11.48	0.01	0.52	Na _{0.26} K _{0.67} Ca _{0.01} Al _{0.99} Si _{3.02} O ₈
CSY-2 (#3)	Xinghe	66.04	0.03	18.31	0.21	0.00	0.08	0.14	1.00	13.29	0.02	0.82	Na _{0.09} K _{0.78} Ca _{0.01} Al _{0.99} Si _{3.04} O ₈
CSY-3 (#4)	Xinghe	65.61	0.01	18.10	0.42	0.01	0.04	0.13	1.73	13.45	0.01	0.54	Na _{0.15} K _{0.79} Ca _{0.01} Al _{0.98} Si _{3.02} O ₈
CHG-2 (#2)	Chifeng	66.16	0.03	18.07	0.31	0.00	0.18	0.30	2.63	11.66	0.01	0.78	Na _{0.23} K _{0.68} Ca _{0.01} Al _{0.98} Si _{3.05} O ₈
CHG-12 (#11)	Chifeng	66.20	0.03	18.37	0.22	0.00	0.13	0.23	2.50	11.43	0.01	0.79	Na _{0.22} K _{0.67} Ca _{0.01} Al _{0.99} Si _{3.03} O ₈

[†] total iron oxide;
LOI: loss on ignition

*all localities are in
Inner Mongolia, China

1400
1401
1402

Table 2. BET (N₂) specific surface areas of orthoclase samples

Sample ID	BET unaltered (m ² /g)	BET altered (m ² /g)
CSY-1C (#6)	3.8	13.7
CSY-2C (#3)	2.1	12.4
CSY-3C (#4)	4.9	13.3
CHG-2C (#2)	2.8	11.1
CHG-12C (#11)	*	*

* insufficient sample available

1403
1404
1405

1406 Table 3. EDXS-measured elemental atomic ratios (unaltered orthoclase
 1407 measured by XRF), and probable secondary phases- when identification
 1408 was not possible, the phases are marked as CASH/CSH + carb (see text).
 1409 Measurement locations in Figs. 4a-c, Fig. 9b, Fig. S7. np = nanoparticles
 1410
 1411

ortho #6	Al/Si	K/Si	Ca/Si	probable phase, remarks
CSY-1C				
1	0.34	0.24	-	orthoclase
2	0.33	0.23	0	orthoclase
3	0.31	0.17	0.01	orthoclase
4	0.21	0.10	0.67	amorphous (?)
5	0.53	0.30	0.02	CASH
6	0.16	0.06	2.60	CASH/CSH + carb
7	0.19	0.01	0.72	CASH/CSH + carb
8	0.15	0.07	0.74	CASH/CSH + carb
Fig. 9b	0.30	0.72	0.32	amorphous SAL
unaltered	0.33	0.22	0.003	$\text{Na}_{0.26}\text{K}_{0.67}\text{Ca}_{0.01}\text{Al}_{0.99}\text{Si}_{3.02}\text{O}_8$
ortho #4				
CSY-3C				
9	0.11	0.12	1.11	CASH+carb
10	-	-	-	resin
11	0.97	0.67	45.43	calcite
12	0.35	0.23	0.001	orthoclase
13	0.25	0.10	0.21	amorphous (?)
14	0.15	1.23	13.42	calcite
15	0.15	0.60	1.26	CASH/CSH + carb + np
16	0.10	0.09	1.10	CASH/CSH + carb + np
17	0.20	0.19	0.35	amorphous (?)
18	0.12	0.005	0.27	CASH/CSH + carb
19	0.18	0.06	1.07	CASH/CSH + carb
20	0.34	0.25	0.002	orthoclase
unaltered	0.32	0.26	0.003	$\text{Na}_{0.15}\text{K}_{0.79}\text{Ca}_{0.01}\text{Al}_{0.98}\text{Si}_{3.02}\text{O}_8$

1412 **Figure Captions**

1413

1414 **Fig. 1.** Experimental protocol flow-chart for alkaline hydrothermal alteration process- see Materials and
1415 Methods, section 2.2 for details.

1416

1417 **Fig. 2.** Field emission scanning electron microscope (FESEM) secondary electron images of a polished
1418 section showing a primary orthoclase grain in cross section after hydrothermal alteration. a) Single grain
1419 (CSY-1C) surrounded by a rim of secondary crystalline phases. b) Close-up of rim (1) and globular
1420 entities (2-4) comprised of an amalgam of secondary phases, including amorphous material, calcite, and
1421 CASH + CSH phases.

1422

1423 **Fig. 3.** Mono-elemental chemical maps measured by FESEM-EDXS (energy dispersive X-ray
1424 spectroscopy) of the same area as in Fig. 2b. The individual elements are indicated at the inner bottom
1425 corners of each image. The white arrows demarcate the interface between orthoclase and the alteration
1426 rim of secondary products. K, Ca, Si, and Al are present at significant concentrations in most of the
1427 secondary globular entities (2-4), whereas Ca is particularly enriched in area 4, and somewhat in the rim
1428 (1)- the high [Ca] in area 4 may point to enrichment in calcite. The majority of C is associated with
1429 resin, and its occurrence in areas 1-4 corresponds in large part to the presence of calcite.

1430

1431 **Fig. 4.** Focused ion beam (FIB) ultrathin sections imaged by high angle annular dark field-scanning
1432 transmission electron microscopy (HAADF-STEM). Rectangles indicate areas of EDXS analyses-
1433 results reported in Table 3. White arrows demarcate the orthoclase interface with secondary products. a)
1434 Cross sectional image reveals both amorphous (4) and crystalline secondary products (5-8) in close
1435 contact with an orthoclase grain (CSY-1C, nos. 1-3). Analysis area of rectangle 8 is only partially
1436 shown. The bladed crystals are likely to be tobermorite. b) Image showing orthoclase grain CSY-3C
1437 (12), calcite (white band, 11), other secondary crystalline phases (9), and resin (10). c) Image of same
1438 interface (CSY-3C) at different location; note the amorphous phase (13) with large pores contacting the
1439 orthoclase interface, the white band is likely a calcite layer (14). The small white particles (lower half of
1440 image, including analyzed areas 15, 16) are presumed to be nano-sized precipitates.

1441

1442 **Fig. 5.** a) Bright field (BF) TEM image of orthoclase grain (CSY-3C) and its interface (dashed white
1443 arrows) with secondary precipitates. Note the bladed crystals (tobermorite), the globular entity (bounded
1444 by 3 white arrows), and a band of calcite (opposing white arrows). The precipitate region is hydrated, as
1445 evidenced by the white globules (e.g., over scale bar) that are likely to be water-rich inclusions. Note

1446 also the abundant small black nano-size grains throughout the precipitate (these appear white in Fig. 4c).
1447 b) Deconvolved spectrum, obtained by selected area electron energy loss spectroscopy (EELS), serves to
1448 identify the calcite band, based on distinct C K (289 eV and 300 eV) and Ca $L_{2,3}$ (348 and 351 eV) edge
1449 structures.

1450

1451 **Fig. 6.** a) BF TEM image of orthoclase grain (CSY-1C) showing well-defined structural and mass-
1452 density interface (white arrows) between crystalline orthoclase and secondary precipitates. b) Ca $L_{2,3}$
1453 energy filtered TEM (EFTEM) 3-window chemical map of the same region at slightly lower
1454 magnification. White areas are Ca-rich, and conversely, black areas are devoid of Ca, such as the
1455 orthoclase grain and resin. Note the sharp change in Ca concentration at the interface. Secondary
1456 precipitates also appear at right edge of image.

1457

1458 **Fig. 7.** EDXS-derived ratios of Na, Na + K, K, and Si, all normalized with respect to Al, as function of
1459 total electron dose, measured with a Titan Themis TEM on various adjacent areas of unaltered
1460 orthoclase. The trends indicate that K, and to a lesser extent Na, are particularly mobile under a TEM
1461 electron beam, indicating that they should be measured with a total electron dose $< 1.5 \text{ pA}\cdot\text{s}\cdot\text{nm}^{-2}$. These
1462 results explain anomalously low K values measured at orthoclase grain edges (see text, also Fig. 4a- area
1463 3).

1464

1465 **Fig. 8.** HAADF-STEM image of a post-reaction orthoclase grain edge with an abutting amorphous
1466 surface altered layer (SAL). The relative thickness profile (in white- based on iterative calculations using
1467 elemental X-ray intensities) indicates a significant change in thickness at interface between the 2 phases.
1468 This image and the accompanying EDXS chemical profiles were obtained with a total electron dose =
1469 $1.4 \text{ pA}\cdot\text{s}\cdot\text{nm}^{-2}$. The 4 elemental ratio profiles reveal quite different behaviors. The K/Al ratio shows a
1470 sudden jump right at the interface, whereas the Na/Al ratio remains constant in both phases. The Si/3Al
1471 and O/8Al profiles remain roughly constant within the orthoclase (ratios ≈ 1), but at the interface the
1472 ratios suddenly start to fluctuate- this may be due to pores or other inhomogeneities in the SAL. At
1473 distances further away from the interface ($< -30 \text{ nm}$), both ratios show a fluctuating but monotonic
1474 increase.

1475

1476 **Fig. 9.** TEM images of the same area as in Fig. 8, but slightly enlarged and cropped. a) HAADF-STEM
1477 image showing a sharp mass-density interface (white arrows) between orthoclase (CSY-1C) and an
1478 amorphous SAL. Note the presence of the large pore in the SAL. b) Superposed HAADF-STEM image

1479 and EDXS chemical maps of K, Ca, and Si (scale bar = 50 nm, applies to panels a) and b). The abrupt
1480 chemical discontinuity between the orthoclase and the SAL (white arrows) is coincident with the sharp
1481 mass-density change. The interface is in particular demarcated by the very sharp change in Si
1482 concentration (blue). The amorphous SAL contacting the orthoclase is particularly K-rich, while further
1483 away it is distinctly enriched in Ca. The rectangle demarcates where an average chemical composition of
1484 the precipitate was determined by EDXS- see text and Table 3). c) Individual elemental EDXS maps-
1485 note the extremely sharp, step function-like drop in Si and Al at the orthoclase (or)- SAL boundary. The
1486 Ca map indicates that this element did not penetrate the orthoclase structure.

1487

1488

1489 **Fig. 10.** Oriented high-resolution TEM (HRTEM) image showing nm-sharp structural interface between
1490 orthoclase (note lattice fringes) and amorphous phase. Image taken on the same interface as in preceding
1491 figure (orthoclase CSY-1C).